Psilocybin collapses visual change detection and drives cortical dynamics toward a state of surprise

R. De Filippo [1,2*], R. Gillis[3†], D. Wyrick[4†], M. Carlson[3†], S. Durand[3], R. C. Peene[3], A. Bawany[3], A. Amaya[3], C. Grasso[3], W. Han[3], J. Kenney[3], C. Kiselycznyk[3], H. Loeffler[3], L. Marks[3], R. Naidoo[3], B. Ouellette[3], L. Suarez[3], J. Swapp[3], T. Johnson[3], J. Weber[3], J. Wilkes[3], P. A. Groblewski[3], A. Williford[3], M. Buice[4], C. Koch[2,5], I. Rembado[2], Jérôme A. Lecoq[3], T. Ott [1*]

[1] Humboldt-Universität zu Berlin, Bernstein Center for Computational Neuroscience Berlin and Institute of Biology, Berlin, Germany .
[2] Allen Institute, Brain and Consciousness, Seattle, WA, USA .
[3] Allen Institute for Neural Dynamics, OpenScope, Seattle, WA, USA .
[4] Allen Institute, Studio D3 / OpenScope, Seattle, WA, USA .
[5] Tiny Blue Dot Foundation, Santa Monica, CA, USA .

*Corresponding author(s). E-mail(s): roberto.de-filippo@bccn-berlin.de; torben.ott@bccn-berlin.de;
†These authors contributed equally to this work.

Abstract

Psilocybin profoundly alters visual perception, yet the neuronal and circuit mechanisms by which it reshapes visual processing remain unclear. Here, we combined large-scale Neuropixels recordings and cell-type-specific optogenetics in head-fixed mice performing a visual change-detection task. Psilocybin severely impaired task performance without overt effects on motor behavior, suggesting a selective disruption of visual processing. At the level of cortical neurons, psilocybin led to a modest reduction in firing rates of layer V neurons but did not impact image identity coding. Contrariwise, psilocybin induced an oscillatory 4-Hz modulation of visually evoked responses that was strongest in somatostatin-expressing (SST) interneurons in the visual cortex. This modulation selectively

targeted neuronal coding of image change rather than image identity. Psilocybin aberrantly recruited change-encoding neuronal ensembles, particularly SST interneurons, following expected images, transiently biasing visual cortex dynamics toward a state of surprise, shifting population activity during stimulus repetitions closer to the trajectories evoked by genuine stimulus changes. Psilocybin-induced modulation was strongest following images with clear, continuous contours, which preferentially recruited change-encoding ensembles. These results demonstrate that psilocybin drives internally generated surprise signals, providing a circuit mechanism for altered perception in the acute psychedelic state.

Keywords: psilocybin, SST neurons, psychedelics, change detection task

Psychedelics such as psilocybin profoundly alter visual perception, producing vivid perceptual experiences and shifts in sensory salience[1–3]. Predictive processing frameworks propose that these effects arise from aberrant perceptual inference, suggesting that psychedelics distort the balance between top-down expectations and bottom-up sensory evidence[4, 5] or directly alter the computation of prediction error signals[6]. A common prediction of these models is an altered capacity to distinguish expected from unexpected visual inputs. However, how psychedelics alter cortical circuit dynamics and specific cell types to disrupt this computation remains unknown. To address this question, we used a visual change-detection task in head-fixed mice that directly tests the ability to detect deviations from learned visual expectations[7, 8] on the Allen Institute *OpenScope Brain Observatory*. In this go/no-go task, mice were presented with a continuous series of eight natural images they had been previously trained on, each flashed for 250 ms and separated by a 500 ms gray-screen inter-stimulus interval. After a variable number of image repetitions ("no-change images"), stimulus identity changed ("change image"), and mice reported the deviant image by licking a water spout to obtain reward (Figure 1A). This design dissociates neural coding of stimulus identity from neural coding of image change. We combined large-scale Neuropixels recordings across the mouse visual hierarchy with optogenetic identification of SST interneurons and psilocybin administration. We focused on SST interneurons because

of their established roles in lateral subtractive inhibition and proposed involvement in prediction error computations[9–12]. This approach allowed us to test how psilocybin impacts the cell-type-specific representations of expected versus unexpected visual information, a key feature of predictive processing.

Neuropixels recordings and behavioral tracking during psilocybin administration

To assess the effect of psilocybin on sensory perception, we trained head-fixed mice (n=10) on a well-established operant visual change-detection task implemented as a standardized, high-throughput pipeline at the Allen Institute [7, 13]. Of the 10 mice trained, 9 performed the task successfully on recording days (perceptual sensitivity above chance in pre-injection epochs, one-sample t-test against 0.5). Performance was evaluated across pre- and post-injection epochs over two consecutive days: mice received saline on day 1 and psilocybin (1 mg/kg, intraperitoneal) on day 2, while two additional control animals received saline on both days (Figure 1B). Before each experiment, intrinsic signal imaging was used to map the borders and retinotopy of visual cortices; these maps then guided probe insertions to record from neurons with receptive fields near the center of the visual stimulus. We then recorded single-unit activity using six Neuropixels probes targeting visual and frontal cortical areas (Figure 1E), while simultaneously tracking licking, running speed, pupil diameter, and motor behavior with frontal and lateral cameras (Figure 1C, D, G). After applying quality-control metrics (according to ref.[7]) and a minimum firing rate threshold of 1 spike/s in both behavioral blocks, we obtained an average of 580 ± 30 and 578 ± 39 cortical neurons across all probes for psilocybin and saline sessions, respectively, for a total of 11,012 neurons (4,049 psilocybin and 6,963 saline neurons; Figure 1E). Here, we only consider cortical neurons. All mice were of the Sst-IRES-Cre genotype; Ai32, enabling optotagging of SST interneurons (Figure S1, n = 1,114 optotagged neurons,

62 ± 5 per session). Fast-spiking (FS) cells were identified based on spike waveform shape (Figure 1F)[14].

Psilocybin selectively impairs performance in the visual change-detection task but not motor behavior

Psilocybin administration drastically decreased the reward rate (Figure 2A, Figure S2A–B). Both hit and false alarm rates were significantly reduced compared to saline controls (hits: post psilocybin = 0.072 ± 0.069, n = 7 sessions versus post saline = 0.724 ± 0.076, n = 12 sessions; false alarms: 0.010 ± 0.007 versus 0.049 ± 0.007; mean ± s.e.m.; two-way repeated-measures ANOVA, condition × epoch interaction: P = 0.002 for hits, P <0.001 for false alarms; Figure 2B). While baseline perceptual sensitivity was high and comparable between both groups prior to injection (saline: AUC = 0.927 ± 0.015; psilocybin: AUC = 0.9 ± 0.023; P = 0.91, post-hoc Šídák test), psilocybin profoundly reduced discriminability during the post-injection epoch, yielding a significant condition × epoch interaction (two-way repeated-measures ANOVA, P = 0.0018; AUC = 0.5371 ± 0.025 for psilocybin versus 0.84 ± 0.032 for saline; post-hoc comparison: P = 0.0016). Indeed, performance following psilocybin administration was statistically indistinguishable from chance (P = 0.21, one-sample t-test against 0.5). Remarkably, a single animal, out of 7, proved resilient to the drug, maintaining baseline-level task performance following psilocybin administration (denoted by a star ⋆ in all plots).

To assess the effect of psilocybin on the autonomic system, we tracked pupil dynamics. Psilocybin evoked a significant increase in normalized pupil area (psilocybin: 1.349 ± 0.063, saline: 1.077 ± 0.039; P = 0.0030, independent t-test; mean ± s.e.m.; Figure 2D), recapitulating well-established clinical observation of mydriasis in humans [15]. Importantly, the profound disruption of goal-directed behavior occurred

without any gross motor deficits. Running speed was unperturbed by the drug (psilocybin: 1.82 ± 0.68 cm/s, saline: 1.26 ± 0.32 cm/s; P = 0.90, Mann-Whitney U test; mean ± s.e.m.; Figure 2E). To capture subtle behavioral phenotypes that might elude macroscopic metrics, we applied an automated motion-sequencing analysis to tracked body parts [16]. This machine-learning approach decomposed multi-feature coordinate trajectories into sub-second, stereotyped behavioral "syllables." Evaluating the microstructure of motor behavior, we failed to find any discernible differences in syllable composition or usage between groups (Figure 2F, Figure S2C–F). Together, these findings rule out generalized motor impairment, pointing instead to other causes, such as altered visual processing or reduced motivation.

Psilocybin induces a visual-evoked oscillation strongest in SST interneurons

To investigate the neural basis of the performance deficit, we first asked whether psilocybin altered average firing rates in cortex. To ensure our population analyses strictly isolated the neural correlates of the drug-induced impairment, the single resilient animal was excluded from all following comparisons, leaving n=6 animals undergoing both saline and psilocybin injections. Consistent with previous reports[17–19], psilocybin reduced the firing rates of regular-spiking (RS) neurons relative to saline (P = 0.002, hierarchical bootstrap; Figure S3A–C). Following injection, firing rates increased by 0.09 ± 0.13 spikes/s under saline but decreased by 1.00 ± 0.25 spikes/s under psilocybin (mean ± s.e.m.; P = 0.004, hierarchical bootstrap). By contrast, the firing rates of FS and SST interneurons remained unaltered across all cortical layers (hierarchical bootstrap). To control for potential subtle behavioral confounds not captured by motion-sequencing, we used FaceMap[20] to extract motor principal components and include them as regressors in a generalized linear model (GLM). After accounting for motor variables, residual firing rate differences showed the same

pattern, confirming that psilocybin selectively suppressed, cortex-wide, RS neuron activity, while leaving FS and SST firing rates unchanged (on average, Figure S3D–E). We next asked whether psilocybin altered visual-evoked activity. To isolate visual processing from reward-related confounds that could arise from differences in task performance, we focused our analysis of the effect of psilocybin exclusively on responses to no-change images. Peri-stimulus time histograms (PSTHs) revealed a pronounced 4 Hz rhythmic modulation following psilocybin administration (Figure 3A–B, Figure S4A–B). This oscillation was evident in both spiking activity and local field potentials (Figure S4C). To quantify this rhythmic modulation, we defined an oscillation (Osc) index by fitting a 4-Hz sine wave to the visual-evoked responses (Figure S4D–E). Psilocybin significantly increased the proportion of oscillation-modulated neurons (Osc neurons, $P = 0.002$, Mann-Whitney U test, Figure 3C). Notably, the single animal that maintained behavioral engagement exhibited minimal induction of these oscillations, with no increase from day 1 to day 2 (Figure 3D, star). Across the population, this robust drug-induced rhythmicity was highly apparent in ΔPSTH heatmaps (Figure 3E, I, M) and in area-averaged ΔPSTHs, with the strongest modulation observed in SST interneurons (Figure 3F, J, N). The modulation was specific to sensory areas (VISp, VISam, VISal, VISa, and SSp-bfd) and was largely absent in frontal regions (Figure 3G, K, O). Due to neuron-type-specific inclusion thresholds, the number of analyzed cortical areas varies across populations (see Methods). Quantification of the Osc index across cortical areas showed that the effect was most pronounced in FS and SST interneurons, and within area VISp (Osc neurons under psilocybin: 35.2% of RS, 45.7% of FS, and 58.9% of SST; Osc neurons under saline: 6.6% of RS, 10.5% of FS, and 9.8% of SST; Figure 3G, K, O). SST interneurons showed the largest group difference in modulation (ΔOsc index=0.55 ± 0.25; Figure 3G, K, O). Notably, while the first two peaks of the modulation coincided with image onset and offset, a third peak became visible during the gray screen period for psilocybin (it was barely

visible in saline controls). Together, these results identify a visual-evoked oscillation, strongest in SST interneurons and visual areas, as a signature of psilocybin's effect on visual processing.

Psilocybin selectively recruits change-encoding neurons during image repetitions

To isolate the neural signals most relevant to the task, we used mutual information during the pre-injection baseline to identify distinct subpopulations of neurons encoding either image identity (MIid) or image change (MIchange). Because both task-relevant visual representations and the drug-induced oscillatory modulation (Figure S5A–B) were predominantly localized within visual cortical areas (VISa, VISal, VISam, and VISp), we focused all subsequent analyses on these regions. To minimize the influence of licking on the encoding of change (MIchange), we restricted this analysis to the first 100 ms following image onset. Within the four visual areas we recorded from, RS neurons strongly encoded image identity (Figure 4A, B), whereas image change encoding was significantly enriched in interneurons (Figure 4D, E), consistent with previous reports [21]. Because both MIid and MIchange distributions were highly skewed, we defined functional ensembles (id- and change-encoding) using the top 20th percentile of each population. This approach isolated the minority of highly tuned neurons occupying the long tail of each distribution (Figure S5C). The degree of overlap between id- and change-encoding populations depended on neuron type. Specifically, of the neurons classified as highly-tuned change-encoding, only 13.8% of FS and 15.1% of SST interneurons co-represented image identity, whereas RS cells showed a 34.8% overlap (Figure S5D). This change-related signaling was independent of licking behavior, as mean firing rates during no-change trials were indistinguishable between false alarms and correct rejections (Figure S5E–F).

We next investigated whether Osc neurons were enriched for the encoding of either

image identity or image change. Compared to the remaining population, all Osc neurons carried significantly higher change information MIchange across all cell types (Figure 4F; RS: P = 0.002; FS: P = 0.004; SST: P = 0.002; Mann-Whitney U test), whereas image id information MIid was indistinguishable between groups (Figure 4C). This difference was consistent across individual brain areas, and especially strong in layer 2/3 (Figure S6).

Examination of PSTHs aligned to no-change trials revealed that psilocybin selectively enhanced the visual onset response of change-encoding neurons, an effect most pronounced within the SST population (Figure 4I, J, Figure S7A–C). Quantifying the injection-induced change in z-scored firing rate within a 10 ms window centered at the peak response confirmed significant elevations under psilocybin relative to saline across all functional cell types (RS: saline = -0.30 ± 0.07 (z-scored firing rate, mean ± s.e.m.), psilocybin = 0.30 ± 0.15, P = 0.0010; FS: saline = 0.02 ± 0.09, psilocybin = 0.69 ± 0.25, P = 0.014; SST: saline = 0.88 ± 0.18, psilocybin = 2.52 ± 0.32, P = 0.0060; bootstrap test). Crucially, this drug-induced enhancement did not apply to image id-encoding neurons, which showed no significant differences in their onset responses to repeated images between the saline and psilocybin conditions (hierarchical bootstrap, P >0.05, Figure 4G, H).

Surprisingly, these task-related signals were related to psilocybin-induced oscillations: a higher degree of image change encoding predicted stronger psilocybin-induced oscillations, with significantly weaker correlation observed for identity encoding (Figure 4K, L). This continuous scaling was prominent in SST neurons (Pearson's r = 0.44) and peaked within VISam (Pearson's r = 0.61), a visual area at the apex of the cortical hierarchy [7, 22]. Significant correlations also emerged in RS neurons within VISal and VISam, and FS neurons in VISam (Figure 4L). Together, these results suggest that an individual neuron's capacity to encode visual change is related to its susceptibility to oscillatory modulation by psilocybin.

To assess whether the psilocybin-induced increase in image change encoding neurons is relevant for visual detection, we investigated single-trial dynamics of neural ensembles. We calculated the *active fraction* of id-encoding and change-encoding neurons, respectively, defined as the proportion of neurons whose response to a given image (0 to 100 ms) exceeded their pre-injection average no-change response (see Methods). To assess the behavioral relevance of this metric, we compared the active fraction of change-encoding neurons between hit and miss trials before injection (pre-injection psilocybin and saline were aggregated into a single epoch). We reasoned that hit trials, representing successful detections, should exhibit greater change-encoding activity. In contrast, misses are inherently heterogeneous, potentially arising from either perceptual failures (lack of detection) or motivational lapses (detection without response). Since motivation-driven misses would presumably still engage change-encoding circuits, any hit-miss difference we observe likely underestimates the true magnitude of the perceptual signal. Despite this conservative bias, hit trials exhibited a significantly higher active fraction than misses (Figure 4M; hit: 0.33 ± 0.03; miss: 0.23 ± 0.02; $P = 0.001$, Mann-Whitney U test), confirming that this neural index tracks behavioral performance. Notably, even on hit trials, only a portion of change-encoding neurons were recruited, and the magnitude of this recruitment varied significantly across individual images ($P < 0.001$, Friedman test). This sparse recruitment may reflect the underlying structure of the neural manifold, whereby individual neurons encode only specific image transitions (e.g., Image $A \rightarrow B$ but not Image $C \rightarrow B$), although the present dataset does not sample sufficient transitions to test this directly. Following psilocybin administration, the active fraction during repeated, no-change images rose, on average, to 56% for approximately 30 min (Figure 4N). This increase was observed across all three neuron types, but was strongest in SST interneurons (Figure 4O; RS: $P = 0.041$; FS: $P = 0.035$; SST: $P = 0.02$). Notably, this aberrant engagement was

restricted to change-encoding circuitry; image id-encoding ensembles, excluding neurons with dual selectivity for both identity and change, exhibited no such increase (Figure S8C–E). Indeed, image id encoding MIid remained stable in id-encoding cells before and after psilocybin administration (Figure S8A–B), consistent with reported preservation of visual selectivity under psilocybin[19]. Receptive field mapping indeed confirmed that spatial tuning properties were unaltered post-injection (Figure S9). In contrast, change-encoding neurons, particularly the SST population, showed a strong negative correlation between the magnitude of oscillatory modulation and the discriminability between pre-injection change responses and post-injection no-change responses (Figure 4P; RS: r = -0.25, P <0.001; FS: r = -0.36, P <0.001; SST: r = -0.59, P <0.001). This reveals that elevated oscillatory modulation tracks a loss of discriminative power, impairing a cell's ability to distinguish expected from unexpected visual inputs. Strikingly, under psilocybin, individual change-encoding neurons exhibited stronger responses to a repeated image than they did to a genuine stimulus change prior to injection, a response reversal observed most prominently within the SST population (Figure S7D–F). In these example neurons, however, post-injection change stimuli evoked even higher firing rates, preserving their relative contrast. Within the change-encoding SST population, the degree of oscillatory modulation significantly correlated with an increase in image identity encoding across all cell types (RS: r = 0.160, P = 0.0172; FS: r = 0.208, P = 0.0156; SST: r = 0.355, P <0.001). Because this psilocybin-induced modulation falls within the 100 ms window critical for decision-making [13], it likely alters visual processing essential for task execution.

To determine whether these neural activity changes were sufficient to disrupt task-variable decoding, we implemented a cross-epoch decoding analysis targeting both image id and image change. To account for session to session variability, we evaluated two decoders: an intra-epoch decoder using 5-fold cross-validation within the pre-injection baseline, and a cross-epoch decoder trained on pre-injection activity

and tested on post-injection activity. Importantly, psilocybin-induced modulation significantly degraded cross-epoch decoding accuracy specifically for distinguishing change versus no-change responses, whereas image id decoding performance was not significantly altered (Figure S10B–F). Because statistical decoders optimize over high-dimensional population variance while completely ignoring the biological constraints that restrict downstream information flow[23], this observed reduction likely underestimates the functional disruption. For the change decoder, significant performance reductions were observed across all functional neuron types, and were selectively localized within area VISam and cortical layer 5 (Figure S10C–G).

Psilocybin shifts population dynamics toward sensory surprise

We next asked whether the altered activity of change-encoding neurons was accompanied by a reorganization of visual cortical population dynamics, bridging our findings across scales. We used principal component analysis (PCA) to track the temporal evolution of population dynamics in a low-dimensional state space following image onset. We hypothesized that the aberrant activation of change-encoding neurons contribute to shifting the entire neuronal population's no-change responses toward states normally evoked by genuine image changes To test this, we focused on early image-onset responses (0–100 ms) and applied PCA to pre-injection data, defining a fixed, low-dimensional subspace that captures the dominant response structure of visual cortex to both change and no-change images. Post-injection no-change responses were then projected into the same PCA space, allowing us to track how psilocybin altered population trajectories. Neural trajectories for change and no-change images diverged across all cell types, as expected[7] (Figure S11). To compare the effects of the injection with genuine image changes on these trajectories, we defined two state-space vectors: the change shift (the difference between pre-injection change and no-change responses),

capturing the population activity induced by a true image change, and the injection shift (the difference between post- and pre-injection no-change responses), measuring the drug-induced modulation. While saline control vectors remained near the origin, indicating that the activity remained largely unchanged following saline injections, psilocybin induced a distinct population shift (Figure 5A). In SST interneurons, this trajectory qualitatively mirrored the path of genuine image changes. To determine whether this displacement aligned with the trajectory of a true stimulus transition, we computed in each session the scalar projection of the injection shift vector onto its corresponding change shift vector to yield a change-alignment index. For both RS and SST neurons, psilocybin significantly increased this index relative to saline controls (RS: $P = 0.0064$; SST: $P = 0.044$) and temporally shuffled baselines (RS: $P = 0.0088$; SST: $P = 0.035$; permutation tests, Figure 5B). Furthermore, in the psilocybin condition change-encoding SST interneurons exhibited, up to 50 ms after image onset, dynamics that matched the precise temporal profile of true image change responses (Figure 5C). Thus, psilocybin transiently redirects cortical population trajectories by driving no-change responses along a pathway that recapitulates genuine visual transitions, an effect most pronounced within SST interneuron populations.

Stimulus features shape psilocybin-induced modulation

Our preceding analyses treated neural responses to the image set collectively by averaging across all eight images. But does psilocybin reconfigure cortical networks uniformly, or do specific stimulus features dictate this modulation? This question is especially salient given that change-encoding ensembles are differentially recruited across individual images. Indeed, we found that the magnitude of psilocybin-induced oscillatory modulation varied substantially across the image set (Figure 6A). Visual inspection suggested that this variability was related to structural image properties,

particularly contour length and density. To quantify this relationship, we defined a Contour Fragmentation Index (CFI) as the ratio of the number of discrete contours to their average length. Under this metric, smooth and continuous contours yield CFI values near zero, whereas highly fragmented contours produce correspondingly large CFI values. This metric predicted the magnitude of psilocybin-induced modulation across these 8 images, accounting for a remarkable 70.2% of the variance (Figure 6B–C). A strong correlation was also observed under saline conditions, even with much smaller Osc values (43% explained variance). We next asked whether this feature dependence reflected the tuning of the ensembles recruited by psilocybin. Change-encoding neurons were highly stimulus-selective, responding on average to only 1.86 $\pm$ 0.04 (mean $\pm$ s.e.m) of the 8 images presented. Consistent with this sparse tuning, the fraction of change-encoding neurons recruited by genuine changes varied across stimuli (min-max range: 0.17 to 0.26; Figure 6D) and inversely correlated with the CFI (Pearson r = 0.60). Moreover, the magnitude of psilocybin-induced modulation was strongly correlated with the size of these image-specific change-encoding ensembles (Pearson r = 0.63; Figure 6F). Thus, the image dependence of the psilocybin effect reflects the selective recruitment of feature-tuned change-encoding neurons.

Together, these findings demonstrate that psilocybin does not trigger a uniform cortical state shift. Instead, this modulation remains constrained by the structural features of the visual input.

Discussion

Our behavioral results demonstrate that 1mg/kg of psilocybin strongly impairs visual change detection in mice with performance falling to chance. Using large-scale single-unit recordings, we found that this deficit was accompaniend by a strong visually-evoked 4-Hz oscillatory modulation, consistent with a recent report[24] and potentially reflecting altered thalamo-cortical interactions[25]. This oscillation was

strongest in change-encoding SST interneurons and transiently shifted population dynamics toward a state evoked by genuine image changes, that is, a surprising sensory stimulus. Notably, the temporal dynamics of this shift mirrored the kinetics of the head-twitch response[26, 27], an established indicator of psychedelic potency in mice[28].

We propose that the shift toward surprise-like neural dynamics directly underlies the observed behavioral impairment. This disruption aligns with both the visual distortions observed in humans under psychedelics[29] and classic evidence that these compounds impair sensory adaptation[1, 30], effectively dismantling the adaptation strategy mice rely on to solve this specific task[13]. More broadly, this disruption of operant performance parallels the suppression of classically conditioned freezing by psilocybin [31], suggesting that psilocybin interferes with the expression of learned behavior across distinct associative paradigms.

First, it is unlikely that the collapse in task performance stems from gross motor deficits, since in-depth video analyses did not reveal any clear impairment or alteration following psilocybin administration. Second, the simultaneous absence of both the behavioral and neural signatures in a single resilient mouse - neither showing a drop in performance nor a strong 4-Hz oscillation - within our cohort suggests that neural and behavioral effects are related. Third, psilocybin is not known to selectively suppress task motivation or engagement[32, 33]. Finally, the behavioral disruption cannot be attributed to a loss of information about image identity. Basic sensory representations were fully preserved: receptive fields remained unchanged, and image-identity could be decoded from the population as accurately under psilocybin as under saline controls. Although a heightened internal bias toward change-signaling might seem paradoxical given the near-complete absence of task attempts, i.e. reduced hits without an increase in false alarms, these observations can be reconciled. We posit that this abnormal internal deviance signaling collapses the high-level contextual priors that

normally guide task-engagement policies, decoupling visual perception from the goal-directed action required by the task.aberrant recruitment of change-related networks impaired the neural contrast between repeated and genuinely changed stimuli, which may leave true changes insufficiently distinct to trigger the learned lick response. these observations can be reconciled if we posit that persistent internal deviance signaling may disrupt visual perception this abnormal internal deviance signaling collapses the high-level contextual priors that normally guide task-engagement policies, decoupling visual perception from the goal-directed action required by the task. We note, however, that a direct causal link between our observed neural signatures to behavioral performance remains to be established.

Current predictive processing models of acute psychedelic effects propose a disruption in the distinction between expected and unexpected sensory signals[4–6]. Our results provide a circuit mechanism for this phenomenon: psilocybin selectively amplifies change-encoding populations, causing even predicted, repeated images to evoke activity shifted toward contextual novelty. This effect was strongest in higher visual areas, notably VISam, and scaled inversely with the contour complexity of the images, indicating that psilocybin perturbs contextual computations according to the image content and the size of the associated change-encoding ensemble.

This circuit-level account is consistent with reports across sensory modalities in mice and humans that psychedelics make responses to predicted and unpredicted stimuli more similar[34–36]. Similarly, in rats, psychedelics made dopamine responses to predicted rewards resemble those to unexpected rewards during learning, consistent with increased prediction-error signaling[37]; earlier behavioral studies in cats likewise reported reduced simple adaptation[1, 30]. At the cellular level, the psilocybin-induced oscillation was strongest in SST interneurons, which have been implicated in encoding sensory-feedback discrepancies[9, 11, 38], navigation errors[10], and sensory adaptation[39–41].which have been linked to the computation of prediction errors

during sensory feedback discrepancies [9, 11] and active navigation errors [10] and adaptation [39–41]. Notably, serotonin, the natural ligand of the 5-HT2A receptor, has been associated with the broadcast of prediction errors and uncertainty [42–45]. Transcriptomic data reveal that some SST subtypes express 5-HT2A receptors[46–48], raising the possibility of direct modulation. While psilocybin has been reported to inhibit SST neurons in the prefrontal cortex [49], psychedelic effects on these inhibitory networks may be highly region-specific or dependent on distinct cellular subtypes. Explanations of psychedelic action have focused predominantly on deep-layer pyramidal neurons[4, 26, 50–52]. Our findings reveal a prominent, previously unappreciated modulation of SST interneurons following psilocybin administration. This mechanism may also help clarify the circuit basis of psychedelic-induced therapeutic effects; altered SST function is a hallmark of depressive disorders and low affect[53–57], which are characterized by rigidly over-weighted contextual priors[58]. By showing that psilocybin acutely alters mechanisms related to contextual novelty, these findings offer a potential circuit mechanism for the visual alterations observed under psychedelics.

Experimental procedures

Data and code availability

The data from all experiments are available for download in Neurodata Without Borders (NWB) format on the DANDI Archive (https://dandiarchive.org/dandiset/001417/draft). All custom code used to analyze this data is available at https://github.com/RobertoDF/psycode.

The following open-source software packages and libraries were used: NumPy, SciPy, scikit-image (skimage), Matplotlib, Pandas, xarray, scikit-learn, DeepLabCut, statsmodels, pingouin, iblatlas, keypoint-moseq, seaborn, joblib, spikeinterface[59], Jupyter (https://jupyter.org/), and pynwb (https://pynwb.readthedocs.io/en/stable/).

Animals

All experiments were performed in Sst-IRES-Cre;Ai32(RCL-ChR2(H134R)_EYFP) mice (n = 10; 7 females and 3 males), aged 5–7 months. All procedures were approved by the Allen Institute's Institutional Animal Care and Use Committee. After surgery, mice were single-housed and maintained on a reverse 12-h light cycle (20–22°C, 30–70% humidity), with experiments conducted during the dark cycle. For behavioral experiments, mice were water-restricted to maintain 85% of their initial body weight, with ad libitum access to food. The cohort consisted of 8 mice assigned to the drug treatment group (Day 1: sterile 0.9% saline; Day 2: psilocybin, 1 mg/kg) and 2 mice assigned to the control group (sterile 0.9% saline on both days). All injections were administered intraperitoneally (i.p.), and Day 1 and Day 2 sessions were consecutive (24 h apart). This design yielded an initial potential pool of 12 saline sessions and 8 psilocybin sessions across the cohort. The psilocybin session for mouse 752309 was excluded entirely from both neural and behavioral analyses due to a synchronization error between the neural data, lick registrations, and visual stimulus timestamps. Task-performance analyses required a pre-injection perceptual sensitivity (AUC) >0.7 on both recording days. Mouse 760322 did not meet this criterion (pre-injection AUC = 0.504 in both its saline and psilocybin sessions). This animal was excluded from the change-detection performance evaluation but was retained for all neural data analyses. Consequently, the behavioral analysis of change-detection performance (Figure 2B, C) included 11 saline sessions from 9 mice, and 6 psilocybin sessions from 6 mice. One saline session was excluded from the running-behavior analysis because of a sensor malfunction.

Single-unit and local field potential recordings

Extracellular single-unit recordings and local field potential recordings using Neuropixels probes was conducted at the Allen Institute as part of the NIH-funded

OpenScope project (https://alleninstitute.org/division/mindscope/openscope/). Mice underwent headplate implantation and craniotomy surgery. The cranial implant was a SHIELD implant described previously in detail[21]. Briefly, we created a CAD file of the implant with holes strategically placed above the areas of interest for our study. Hole positions were adjusted using Pinpoint[60]. Approximately a week after surgery, intrinsic signal imaging was used to identify visual area boundaries[61]. The mice were then habituated and trained in the behavior setups for several weeks and then to the Neuropixels rigs every day for a week. To prepare the brain for electrophysiological recordings, the coating over the implant was removed and replaced with a temporary layer of Kwik-Cast (World Precision Instruments). This was done a few days prior to recording to avoid using isoflurane the day of the experiment.

On the day of recording, the mouse was head-fixed, the protective well cap and Kwik-Cast layer were removed, and a layer of agarose or silicone oil was applied[62]. Six Neuropixels 1.0 probes[63] were targeted to visual areas (VISp, VISal, VISam, VISa), anterior cingulate (ACA), and primary somatosensory cortex (SSp-bfd). Probes were coated with CM-DiI (1 mM in ethanol; Thermo Fisher Scientific, V22888) for post-hoc localization. Each probe was mounted on a 3-axis micromanipulator (New Scale Technologies), aligned to its target opening, and manually lowered to the brain surface. After initial penetration (~100 μm), probes were inserted automatically at 200 μm min^{-1} to a final depth of $\leq$3.5 mm and allowed to settle for 15–30 min.

Data were acquired at 30 kHz (spike band, 500-Hz high-pass) and 2.5 kHz (LFP band, 1,000-Hz low-pass) using the Open Ephys GUI[64]. Videos of eye and body were acquired at 30 Hz; running wheel angular velocity was recorded at ~60 Hz. Spike-band data were median-subtracted and processed with Kilosort4 [65]. Quality labels were computed for each putative neuron using UnitRefine[66]. Putative double-counted spikes (spikeinterface.curation.remove_duplicated_spikes) and artefactual units were removed (noise label by UnitRefine); remaining units were packaged into Neurodata Without Borders files.

We used published protocols to prepare whole mouse brains for clearing. Briefly, brains were perfused and fixed in 4% paraformaldehyde for light-sheet microscopy. In a timeline of two weeks, the brain was stripped of lipids ([67]) and rendered transparent in an index matching solution ([68]), allowing for viewing the morphology of anatomical brain structures. Brains were then embedded in agarose for imaging ([69]). This protocol collection is ideal for experiments where it is necessary to preserve endogenous fluorescence. Agarose blocks containing cleared mouse brains were imaged by a light sheet microscope (LifeCanvas Technologies).

After the brains were processed in the imaging pipeline, Neuroglancer (https://Neuroglancer-demo.appspot.com) was used to reconstruct probe tracks in the brain. Points were placed along the length of the probe track and were closely inspected to ensure annotation of the probe tip and each track is assigned to a particular day of recording. Electrophysiological features recorded from neural probes were aligned with anatomical landmarks based on the Allen Mouse Brain Common Coordinate Framework (CCFv3) (Wang et al. 2020). For this, we used the IBL alignment GUI (https://github.com/AllenNeuralDynamics/ibl-ephys-alignment-gui).

Optotagging to identify SST interneurons

Following receptive field mapping and behavioral task (see below), the same optotagging procedure was performed on all mice. Blue light was delivered via a 465 nm LED (Plexon) controlled by a Cyclops LED driver or a 473 nm laser (Laser Quantum Ciel or Cobolt 06-MLD). The light source was coupled to a 400 µm diameter fiber optic cable (Thorlabs), with the tip positioned to illuminate the cranial window located in visual cortex. The following three stimulus types were presented at each of three light levels, with all nine combinations randomly interleaved: 6 ms pulses at 10 Hz, 10 ms pulses at 5 Hz, and a 1 s raised cosine ramp. Stimuli were presented at intervals of 1.5 s plus a uniformly distributed delay of 0–0.5 s. Mice had no prior exposure to the

optotagging stimulus before the recording session. Optotagged cells were identified based on their responses to the 5 Hz stimulation. For each neuron, we examined each pulse individually. For every pulse, we calculated the firing rate in a 10-ms window beginning 2 ms after pulse onset and compared it to the number of spikes in a baseline window from –11 to –1 ms before pulse onset. A Wilcoxon signed-rank test was then applied across all pulses to determine whether post-stimulus and baseline spike counts differed significantly. Because some pulses yielded zero spike counts in both windows, we used a zero-handling method (zero_method='zsplit' in scipy.stats.wilcoxon) that splits ties equally between positive and negative ranks, providing a balanced treatment of zero differences. Neurons with a significant difference (two-sided $p < 0.05$) were classified as SST neurons.

Change detection task

Mice were trained in custom-designed, sound-attenuating behavior enclosures equipped with a 24 gamma-corrected LCD monitor (ASUS PA248Q). Head-fixed mice were positioned on a behavior stage with a 6.5 running wheel tilted upward by 10–15°. The monitor was placed 15 cm from the right eye, and visual stimuli were spherically warped to maintain constant perceived size, speed, and spatial frequency across the visual field. Water rewards were delivered via a solenoid (NI Research, 161K011) through a blunted 17-gauge hypodermic needle (Hamilton) positioned 2–3 mm from the animal's mouth.

Mice were trained 1 h/day, 5 days/week on a go/no-go change detection task (Figure 1A). Mice learned to lick a reward spout when the identity of a briefly flashed visual stimulus changed. Correct responses within a post-change window (150–750 ms) triggered a water reward. Each session consisted of a continuous series of images. Change times were drawn from a truncated exponential distribution ranging from 2.25 s to 8.25 s (mean=4.25 s) following sequence onset.

Each image presentation was treated as an individual trial. On each trial, the animal's licking behavior was classified relative to the trial type (change vs. non-change). A hit was defined as a lick on a change trial in a window up to 0.9 s after image onset, a miss as no-lick on a change trial, a false alarm as a lick on a non-change trial in a window up to 0.9 s after image onset, and a correct rejection as no-lick on a non-change trial. False alarms were assigned only at least 4 images away from a change image to avoid miscategorization of reward-licks. For each session and each experimental epoch (e.g., pre-injection, post-injection), the proportion of each outcome was calculated separately for change image and no-change image trials. Specifically, hit and miss proportions were computed within change trials (hit rate + miss rate = 1), and false alarm and correct rejection proportions within non-change trials (false alarm rate + correct rejection rate = 1). To assess the effect of the drug manipulation on behavioral performance, a two-way repeated-measures analysis of variance (RM-ANOVA) was conducted separately for hit rates (image change trials) and false alarm rates (no-change trials). The within-subject factors were condition (saline vs. psilocybin) and epoch (pre-injection vs. post-injection). The dependent variable was the proportion of hits or false alarms per session. The analysis was performed using the rm_anova function from the Pingouin library (Vallat, 2018). The main statistic of interest was the condition × epoch interaction effect, which indicates whether the change in performance from pre- to post-injection differed between drug conditions.

Motion sequencing analysis

Body part tracking was performed with DeepLabCut (version 3.0.0rc10)[70]. We labeled 109 frames from a frontal video and 99 frames from a lateral video for training (both 658×792 pixels, 60 fps). The following keypoints (body features) at the frontal camera were defined: frontpaw left, frontpaw right, hindpaw left, nose base, nose tip, ear base, ear mid. For the lateral camera, we used the following keypoints: frontpaw

left, frontpaw right, hindpaw left, hindpaw right, tail base, tail mid, tail tip, nose tip, ear tip. 95% of frames were used for training a ResNet-101 network (default parameters, 200 iterations, 5 shuffles) with the following parameters: Training error, 1.06 pixels (frontal) and 2.23 pixels (lateral); test error, 5.7 pixels (frontal) and 4.6 pixels (lateral); cutoff p-value = 0.1 for both x and y coordinates before modeling.

Unsupervised behavioral classification used Keypoint-MoSeq (v0.6.7)[16]. Outlier keypoints were removed (scale factor = 6.0). PCA on aligned, centered keypoints selected 5 latent dimensions (minimum explaining 90% variance). Kappa was tuned to 106 (autoregressive-only model) and 105 (full model) to achieve a median syllable duration of more than 10 frames. After fitting the AR-HMM, the model was reapplied to training and new data. Syllable frequency and duration were analyzed with MoSeq's function 'plot_syll_stats_with_sem' setting a minimum syllable frequency of 0.01 and restricting the analysis to post-injection epochs.

Single-unit analysis

Following automated spike sorting, units were classified using UnitRefine[66], an automated curation framework trained to reproduce expert labels by integrating complementary features of spike timing, waveform morphology, amplitude stability, and cluster isolation. UnitRefine assigned each cluster to single-unit activity (SUA), multi-unit activity (MUA), or noise. Units were retained if they were classified as SUA or, if they met the following quality metrics: ISI violations <0.5 (the relative firing rate of contaminating spikes, estimated from interspike intervals shorter than 1.5 ms and normalized by the overall spike rate), amplitude cutoff <0.1 (an estimate of the fraction of spikes missed because their amplitudes fell below the detection threshold, calculated from the symmetry of the spike-amplitude distribution), and presence ratio >0.9 (the fraction of 100 equal-duration recording blocks containing at least one spike from the unit; values above 0.9 indicate detection in more than 90% of the session).

Only units with a firing rate of at least 1 spike/s in both the pre- and post-injection behavioral epochs were included. These thresholds ensured well-isolated, stable units with minimal contamination from multi-unit activity. Optotagged SST interneurons were included regardless of these thresholds, as their identity was independently confirmed by light-evoked responses. Fast-spiking (FS) neurons were identified based on a trough-to-peak latency <0.4 ms.

For population-level comparisons across conditions, additional inclusion criteria were applied to ensure robust statistical power. For RS and FS neurons, cortical areas were included only if they contributed at least three sessions per condition (saline and psilocybin), with each session containing at least seven neurons of that type. For the sparser SST population, areas were included if they had at least three sessions per condition with a minimum of four neurons per session. These thresholds balanced statistical power with the retention of as many areas as possible given the lower yield of interneurons.

For each isolated unit, spike density functions (SDFs) were computed across a temporal window of -1.0 to 1.5 s relative to either the image change or the regular image flash immediately preceding it ("pre-change"). Spike trains were binned at 1 ms resolution and convolved along the temporal axis with a causal, right-aligned exponential filter window:

$$K(t) = \begin{cases} \exp\left(-\frac{t}{\tau}\right) & \text{for } t \geq 0 \\ 0 & \text{for } t < 0 \end{cases} \tag{1}$$

where the decay time constant was set to $\tau = 5$ ms. The resulting convolved arrays were divided by the sampling interval to convert counts to firing rates (spikes/s). To normalize firing rates, z-scoring was performed using baseline statistics (mean and standard deviation) computed from the entire pre-injection change-detection block, the full behavioral session before drug administration. This extended window provided stable estimates even for neurons with extremely sparse firing. The same pre-injection

statistics were used to normalize spike counts during all stimulus periods (both pre- and post-injection), expressing each neuron's responses relative to its own pre-injection baseline.

GLM-based residual analysis for behavioral confounds of neural activity changes

To control for behavioral confounds regarding psilocybin-induced neural activity changes, we built a generalized linear model (GLM) for each neuron using the 'PopulationGLM' implementation from the nemos library (https://github.com/flatironinstitute/nemos). For each session, we extracted the first 60 principal components from each of three video-derived streams (face, whisker region, and body) using FaceMap[20]. The whisker video was a cropped version of the face video, created because motion energy in the face video was dominated by paw movements, making it necessary to isolate whisker-specific motion for more precise behavioral tracking. These PCs served as predictors, capturing ongoing motor behavior. Stimulus regressors were intentionally omitted because visual stimuli were identical across pre- and post-injection epochs and across drug and saline groups; any stimulus-driven neural activity would be present in both conditions and thus would not confound drug comparisons. Our goal was not maximal prediction accuracy but isolation of neural activity unexplained by behavior.

The model was trained on pre-injection single-unit firing rates data ending 120 s before injection, to avoid activity elicited by the handling of the animal by the experimenter, using a Poisson likelihood with Lasso regularizer (regularization strength=0.01). After fitting, it predicted firing rates beginning 120 s after injection from the corresponding post-injection behavioral PCs. Pearson residuals were

computed for each 1-s time bin as

$$\frac{\text{observed} - \text{predicted}}{\sqrt{\text{predicted} + \varepsilon}} \tag{2}$$

for each time bin, where ϵ is a small constant (10^{-8}) added to prevent division by zero when predicted rates are near zero. A negative residual indicated less firing than expected by the GLM. Pearson residuals were smoothed with a centered 120-s rolling mean and sampled every 30 s. For each session, brain area, and neuron class, we then computed the median residual across the available neurons, providing a robust, outlier-insensitive summary of neural activity unexplained by behavior.

Oscillation index

To quantify the psilocybin-induced oscillatory modulation on a single-neuron level, we calculated the ΔPSTH as the difference between the post-injection and pre-injection peri-stimulus time histograms, z-scored for each individual neuron. After smoothing each ΔPSTH with a centered 50-ms Gaussian window (SD = 10 ms), a cosine function was fitted to its ΔPSTH over the interval of 0–750 ms post-stimulus onset using nonlinear least-squares optimization (Levenberg-Marquardt algorithm, implemented via scipy.optimize.curve_fit). The model was defined as:

$$f(t) = \beta_0 + \alpha \cos(2\pi \cdot 4t + \phi) \tag{3}$$

where β_0 is the baseline offset, α is the modulation amplitude, and ϕ is the phase. To ensure a standardized representation where the amplitude is strictly positive, if a negative α was returned, we inverted its sign and advanced the phase by π ($\phi \leftarrow \phi + \pi$). We then evaluated the model residuals as the difference between the empirical ΔPSTH and the fitted curve $f(t)$. Fit quality (Q) was defined as the ratio of the amplitude to

the standard deviation of these residuals:

$$Q = \frac{\alpha}{\sigma_{\text{residuals}}} \tag{4}$$

We then defined the Osc index as the fitted amplitude multiplied by a logistic weight determined by (Q):

$$\text{Oscillation Strength} = \frac{\alpha}{1 + e^{-k(Q - s_0)}} \tag{5}$$

with (s_0=0.5) and (k=15), i.e., Osc index = alpha * Q. These parameters produce a steep transition around (Q=0.5), strongly attenuating the amplitudes of fits whose residual variability is large relative to the fitted oscillatory component while preserving the amplitudes of well-fitting 4-Hz oscillations. Thus, the Osc index represents the magnitude of the fitted 4-Hz modulation weighted by its signal-to-residual ratio, rather than a formal measure of statistical significance. To verify that rhythmic modulation included a sustained third peak, we isolated the late-phase window (500–750 ms), repeated this segment three times to span 750 ms, and fit the same model to obtain the late-Osc index. Neurons were classified as oscillatory ('Osc neurons') if both their Osc index and late-Osc index exceeded a threshold defined as the 80th percentile of the Osc index across all cortical neurons in the psilocybin condition.

Mutual information analysis

To quantify the information each neuron carried about image identity and image change, we computed mutual information (MI) between spike counts of the respective categorical variables. For image change encoding, the target variable was a binary vector indicating whether a trial was a change trial (image identity different from the previous reference) or a non-change trial (repetition of the reference image). For

image identity encoding, the target variable was the specific image identity (image id 1–8). Both MI values were computed using the mutual_info_classif function from scikit-learn[71], which is appropriate for discrete features and targets.

Spike counts were extracted per image presentation from both pre and post-injection epochs. For change encoding, we used the early post-stimulus window (0–100 ms after image onset) to capture the rapid detection of a deviation while minimizing potential contamination from reward-related activity. For identity encoding, we used the full stimulus window (0–250 ms after image onset) to capture the sustained representation of the natural image.

Neurons were classified as image change-encoding or image id-encoding if their MI value fell above the 80th percentile of the respective distribution across the population (cf. Figure S5). This threshold was calculated focusing on areas with significant visual information encoding (VISa, VISal, VISam, VISp).

Receptive field analysis

Each experiment included two receptive field mapping blocks, one before and one after injection. Both used drifting Gabor patches (2 Hz, 0.04 cycles/degree) within a 20° circular mask, presented randomly at 81 screen locations (9 × 9 grid) for 250 ms each without blank intervals. To map the spatial receptive fields (RFs) of isolated single units, mean evoked spike rates were quantified as a function of the horizontal (x) and vertical (y) coordinates of the visual stimulus. For each unit, spike times were isolated following individual stimulus presentation trials. Because stimuli were presented continuously with no inter-stimulus interval (ISI = 0 s), the analysis window (Δt) was conservatively truncated to 0.24 s following stimulus onset, which is 10 ms shorter than the nominal 0.25 s stimulus duration. This buffer was introduced to prevent temporal bleed-through and ensure that spike counts were not contaminated by boundary responses to successive stimulus frames. The mean firing rate R(x, y)

for each discrete spatial coordinate was calculated as follows:

$$R(x,y) = \frac{1}{N_{x,y} \cdot \Delta t} \sum_{k=1}^{N_{x,y}} n_k(x,y) \tag{6}$$

where N_x,y is the total number of trials presenting the stimulus at coordinate (x, y), and n_k(x, y) is the number of spikes recorded during trial k within the truncated window Δt = 0.24 s. This procedure yielded a two-dimensional spatial response matrix representing the raw receptive field topology. To isolate structured receptive fields from stochastic background activity, a two-stage non-parametric permutation test was implemented using circular shuffling of spike times. This shuffling mechanism shifted spike sequences randomly relative to stimulus onsets while preserving the intrinsic temporal dynamics of individual units. In the initial screening stage, spike times were subjected to 800 independent circular shuffles across the experimental duration to construct a baseline null distribution. For each shuffle, the spatial response matrix was recomputed. Units exhibiting no spatial pixels above an uncorrected significance threshold of $\alpha = 0.15$ were classified as non-responsive or lacking a structured RF, and were excluded from downstream parametric modeling. In the strict evaluation stage, for units passing the initial screen, a rigorous null distribution was generated via 8000 independent circular shuffles. For each spatial pixel, a two-tailed p-value was calculated by evaluating the proportion of shuffles where the absolute deviation of the null firing rate from the null mean exceeded or equaled the observed absolute deviation from the null mean:

$$P = \frac{N_{\text{shuff}}(|R_{\text{shuff}} - \mu_{\text{null}}| \geq |R_{\text{obs}} - \mu_{\text{null}}|) + 1}{N_{\text{total}} + 1} \tag{7}$$

where R_obs is the observed pixel firing rate, μ_null is the mean of the permutation distribution for that pixel, and N_total = 8000. To control for type I errors across the

spatial grid, the resulting p-value matrix was corrected for multiple comparisons using the Benjamini-Hochberg False Discovery Rate (FDR) procedure with a significance threshold of $\alpha = 0.05$, generating a binary significance mask. The geometric structure of statistically significant receptive fields was characterized by fitting a parametric, rotated 2D Gaussian function to the raw spatial response matrix. The initial center of the fit was localized by finding the peak coordinate of the spatially smoothed significance matrix. Optimization was performed via nonlinear least-squares minimization using the Trust Region Reflective algorithm, utilizing a robust soft L1 loss function to minimize sensitivity to outlier pixel values. The fitted surface was defined by the following objective function:

$$f(x, y) = A \exp\left(-\left[a(x - x_0)^2 + 2b(x - x_0)(y - y_0) + c(y - y_0)^2\right]\right) + B \tag{8}$$

The spatial parameters were constrained by the rotation angle θ (converted to radians) and the spatial standard deviations (σx, σy) along the orthogonal axes:

$$a = \frac{\cos^2\theta}{2\sigma_x^2} + \frac{\sin^2\theta}{2\sigma_y^2} \tag{9}$$

$$b = -\frac{\sin 2\theta}{4\sigma_x^2} + \frac{\sin 2\theta}{4\sigma_y^2} \tag{10}$$

$$c = \frac{\sin^2\theta}{2\sigma_x^2} + \frac{\cos^2\theta}{2\sigma_y^2} \tag{11}$$

where A represents the peak response amplitude, B is the baseline offset, and (x0, y0) defines the fitted parametric center. Goodness-of-fit was penalized for model complexity and quantified using the adjusted coefficient of determination (adjusted R^2). To supplement the parametric model, a scale-invariant, non-parametric eExtremity Index was computed to assess the global salience of spatial tuning over the entire response matrix. This index utilizes a modified zZ-score framework based on median

absolute deviation (MAD) to ensure robustness against localized baseline noise:

$$\text{Extremity Index} = 0.6745 \times \frac{\max(|\mathbf{R} - \tilde{R}|)}{\text{MAD} + \epsilon} \tag{12}$$

where R represents the vector of all pixel values in the response matrix, R is the median firing rate across the entire matrix, $\epsilon = 10\hat{}{-}10$ is a stabilizing constant to prevent zero division, and MAD is defined as:

$$\text{MAD} = \text{median}(|\mathbf{R} - \tilde{R}|) \tag{13}$$

For each unit, we extracted the minimum, maximum, and mean spatial firing rates to capture background and peak activity. For each unit, the processing pipeline extracted a profile of spatial tuning attributes, which were organized into the following distinct parameters: RF center X and RF center Y: The empirical spatial coordinates of the receptive field center, defined as the peak position of the spatially smoothed, FDR-corrected significance matrix.RF width: The maximum continuous spatial extent of the receptive field, calculated by measuring the largest continuous cluster size after convolving the binary significance mask with an 8-connected neighborhood kernel.Sign: The operational direction of the receptive field response inside the significant zone, labeled as positive (excitatory/ON-like response) if the mean z-scored firing rate within the mask is above zero, or negative (inhibitory/OFF-like) if it is below zero.x0 and y0: The mathematical center coordinates of the idealized 2D Gaussian surface, which incorporates the entire shape of the response across the grid rather than just a single peak pixel.σx and σy: The optimized spatial standard deviations along the primary orthogonal axes of the receptive field, explicitly dictating how wide or narrow the tuning profile stretches.Orientation: The rotation angle of

the Gaussian major axis in degrees, capturing the structural tilt or slant of the receptive field profile in visual space.Aspect ratio: A metric tracking the elongation of the receptive field shape, calculated as the ratio of the larger spatial standard deviation to the smaller one, defined as max(σx, σy) / min(σx, σy).Ellipticity: An alternative measure of circular distortion ranging from 0 (perfectly circular) to 1 (highly elongated), defined mathematically as 1 - min(σx, σy) / max(σx, σy).Adjusted R^2: The adjusted coefficient of determination, which quantifies how much spatial variance the 2D Gaussian model accounts for relative to the raw data matrix while penalizing for the number of free parameters.Extremity index: A scale-invariant metric of tuning salience calculated using the median absolute deviation, functioning as a robust, non-parametric z-score that determines how many standard deviations the peak pixel sits away from the global noise floor. Mean firing rate: The average baseline firing rate of the unit calculated uniformly across all stimulus positions in the matrix.Min firing rate: The minimum firing rate recorded at any single spatial position in the matrix, capturing the baseline floor of the neural response.Max firing rate: The maximum firing rate recorded at any single spatial position in the matrix, pinpointing the raw peak response.

Population decoding

To investigate how neural ensembles represent task variables and visual features across drug conditions, we used a population decoding pipeline. We constructed balanced-class linear classifiers applied to spike counts starting from stimulus onset over progressively longer windows. Spike counts were integrated across a grid of temporal parameters with window durations ranging from 10 to 300 ms in 10-ms increments, beginning at stimulus onset. Population decoding was performed using a logistic regression model implemented via scikit-learn. To account for unequal trial distribution across decoded classes, class weights were inversely proportional to class

frequencies:

$$w_c = \frac{n_{\text{samples}}}{n_{\text{classes}} \times n_c} \tag{14}$$

Feature matrices were normalized (z-scored) across trials before model fitting. The pipeline decoded two primary target variables. For image change decoding, a binary classification determined whether a stimulus presentation constituted a change event ("is_change" in stimulus presentation dataframe). For stimulus identity, a multiclass classification identified the specific visual image presented ("image_name" in stimulus presentation dataframe). Models were evaluated using two distinct cross-validation strategies to assess the stability of neural representations. The within-block decoding strategy handled single-epoch decoding by utilizing a stratified k-fold cross-validation scheme where k = 5 to approximately preserve class proportions in each fold. Alternatively, the cross-block decoding strategy assessed the stability of representations across behavior by training models on data from the baseline pre-injection epoch and testing on data from the post-injection epoch. To directly quantify the stability of the population code across these epochs, we calculated the 'generalization Δ', defined as the drop in decoding accuracy between the baseline within-block decoder and the cross-block decoder. Performance for both strategies was quantified using balanced decoding accuracy to guard against any residual class imbalances. To evaluate statistical differences in the temporal trajectory of decoding performance between saline and drug conditions, independent two-sample t-tests (assuming equal variance) were performed to compare generalization Δ values between the saline and psilocybin injection groups within each temporal window. To control for the inflation of type I errors resulting from family-wise testing across the time-window grid, the set of p-values across all unique temporal windows was adjusted for multiple comparisons using the Benjamini-Hochberg false discovery rate (FDR) procedure.

Population trajectory analysis

To assess whether psilocybin reconfigured population-level image or image change representations, we analyzed the time-varying activity of simultaneously recorded neural populations across experimental epochs (pre- versus post-injection), drug conditions (saline versus psilocybin), and trial types (change versus no-change). For each session, cell type, and condition, PSTHs were constructed by aligning spiking activity to image onset over a window of 0 to 100 ms, and z-scored on a per-neuron basis. Only sessions with at least 20 neurons of a given cell type were retained for this analysis. For visualization purposes across this 0 to 100 ms epoch, we built a population matrix by concatenating all neurons from all sessions of a given condition and cell type. To capture the dominant response patterns in our neural ensembles, we applied PCA based on the pre-injection data (change and no-change trials combined). The first three PCs were used to project all conditions into a shared low-dimensional space (Figure S11). This projection provides an intuitive view of the population trajectories. The quantitative analysis was performed in the full, neuron-dimensional space without dimensionality reduction, using the z-scored PSTHs directly. For each session and cell type, we defined two time-resolved difference vectors:

$$\mathbf{v}_{\text{change}}(t) = \mathbf{x}_{\text{pre, change}}(t) - \mathbf{x}_{\text{pre, no-change}}(t) \tag{15}$$

$$\mathbf{v}_{\text{drug}}(t) = \mathbf{x}_{\text{post, no-change}}(t) - \mathbf{x}_{\text{pre, no-change}}(t) \tag{16}$$

where $\mathbf{x}(t)$ represents the population vector (with a length equal to the number of neurons) at time t. At each time point, we computed the scalar projection of the drug-effect vector onto the direction of the image-change vector:

$$\text{Proj}(t) = \frac{\mathbf{v}_{\text{drug}}(t) \cdot \mathbf{v}_{\text{change}}(t)}{\|\mathbf{v}_{\text{change}}(t)\|_2} \tag{17}$$

This projection measures how strongly, and in which direction, the drug shifts the population along the endogenous image-change axis. To obtain a single score per session, the time-resolved projection was averaged over an analysis window of 20 to 80 ms after image onset. Finally, this integrated score was divided by the number of neurons in that session to yield the mean projection per neuron (expressed in arbitrary units, denoted as "Change-alignment (a.u.)"), making sessions with different neuron yields directly comparable. For psilocybin sessions, a null distribution was generated via a temporal shuffle procedure. For each shuffle iteration (1,000 iterations), the time indices of the complete drug-effect trajectory $\mathbf{v}_{\text{drug}}(t)$ were randomly permuted across the entire PSTH epoch prior to window selection, leaving the sensory-change trajectory $\mathbf{v}_{\text{change}}(t)$ intact. This procedure breaks the true time-resolved relationship between the two trajectories while fully preserving the underlying population structure, cell identities, and response amplitudes. The mean projection per neuron was then recomputed for each iteration over the same 20 to 80 ms analysis window. The average across these shuffle iterations defined the session-wise chance level. Statistical significance of the difference between the saline and psilocybin cohorts was assessed using a two-sample permutation test (20,000 iterations) on the per-session mean projection per neuron, performed independently for each cell type.

Image contour analysis

To quantify the contours of the natural images used in the change-detection task, we developed a Contour Fragmentation Index (CFI). This metric captures the degree to which an image is composed of numerous, short, or disjointed edges, which we hypothesized would scale with the recruitment of change-signaling ensembles. The CFI is calculated as the ratio of the total number of discrete contours (N) to their average spatial length ($\bar{L}$):

$$\text{CFI} = \frac{N}{\bar{L}} \tag{18}$$

We implemented a multi-threshold framework to extract contours across diverse luminance levels. Images were first smoothed using a Gaussian filter ($\sigma = 2.0$ pixels) to mitigate high-frequency noise. We then determined a set of optimal intensity thresholds using the Multi-Otsu algorithm configured for four classes. For each identified threshold, contours were extracted from both the original luminance maps and their inverted negative images via the marching squares algorithm (skimage.measure.find_contours). This dual-polarity approach ensured that the index comprehensively accounted for both light-on-dark and dark-on-light structural elements across the full dynamic range of the stimulus. The resulting CFI provides a scalar measurement of image fragmentation; a higher CFI indicates a complex composition dominated by many small, disjointed features, whereas a lower CFI tracks an image with fewer, more continuous structural elements. We then used linear regression to evaluate the relationship between the CFI of each stimulus and its corresponding magnitude of psilocybin-induced neural modulation.

Active fraction analysis

To examine whether psilocybin modulated the recruitment of functional ensembles (either change- or identity-encoding) across sequential trial presentations, we calculated the active fraction of image id-encoding and image change-encoding neurons, defined as the proportion of neurons within an ensemble that were significantly activated on a single-trial basis. For image change-encoding ensembles, candidate neurons were initially selected if the MI between their spike counts and the trial type (change versus no-change) exceeded the 70th percentile of the population distribution. To ensure strict image specificity, these candidate units were then subjected to a secondary, more stringent binomial test ($P < 0.05$) paired with a minimum absolute response difference constraint of 10 spikes/s within a 0-100 ms post-stimulus window. Specifically, we tested whether a neuron's response on a change trial with a given

image was significantly greater than its response on no-change trials where that same image was repeated. Neurons meeting these dual criteria were classified as dedicated change-encoding cells for that specific image identity, capturing the localized tuning of change responses. Conversely, for image id-encoding ensembles, this secondary image-specific filtering was omitted. Instead, selection was restricted to neurons that uniquely encoded image identity, explicitly excluding any units exhibiting dual encoding to both identity and change. Neuronal responsiveness was determined on a trial-by-trial basis for each image presentation by quantifying spike counts within the 0-100 ms window following image onset.For each neuron-image pair, an initial baseline activation threshold (θ_{pre}) was established using pre-injection no-change trials:

$$\theta_{\text{pre}} = \mu_{\text{pre}} + 2\sigma_{\text{pre}} \tag{19}$$

where μ_{pre} and σ_{pre} represent the mean and standard deviation of the post-stimulus spike count across pre-injection no-change trials, respectively. To account for state-dependent fluctuations or baseline firing rate drift over the course of an extended recording session, post-injection thresholds were adjusted dynamically:. the baseline firing rate for each neuron (μ_{baseline}) was calculated within a 250 ms pre-stimulus window, evaluated separately for the pre- and post-injection blocks. The difference between these pre-stimulus baselines was then added to the initial threshold to yield a drift-corrected post-injection threshold (θ_{post}):

$$\theta_{\text{post}} = \theta_{\text{pre}} + (\mu_{\text{baseline, post}} - \mu_{\text{baseline, pre}}) \tag{20}$$

A neuron was classified as active on any given trial if its post-stimulus spike count exceeded its corresponding image-specific, drift-corrected threshold (θ_{pre} for pre-injection trials and θ_{post} for post-injection trials). The active fraction was computed

trial-by-trial as the proportion of responsive neurons within the target ensemble. This metric was calculated separately for the pre- and post-injection epochs to generate a continuous time series aligned to the moment of injection. Population-level time courses were constructed by aggregating these time series across sessions. For each temporal bin, the mean active fraction was compared between the saline and psilocybin conditions using an independent-samples, two-tailed t-test. Normality was verified for the majority of bins; in instances where the normality assumption was violated, statistical significance was confirmed using non-parametric Mann-Whitney- U tests.

Statistical analysis

Statistical analyses were performed in Python (version 3.11) using the scipy.stats, statsmodels, and pingouin libraries. All statistical tests were two-sided unless noted otherwise, and the baseline significance threshold for all analyses was set at $\alpha = 0.05$. Statistical significance is denoted as follows: *(P <0.05), **(P <0.01), and ***(P <0.001).

Hierarchical bootstrap

To account for the nested structure of the neural recordings, where hundreds of individual neurons were sampled across a smaller cohort of sessions, we implemented a hierarchical bootstrapping approach to evaluate population-level metrics. This framework avoids the inflation of statistical significance that occurs when treating individual cells as independent samples. For each comparison, we executed 10,000 bootstrap iterations. On each iteration, experimental sessions were first resampled with replacement, and the constituent neurons within those selected sessions were subsequently resampled with replacement. This bootstrap distribution was used to derive the population mean and the standard error of the mean (s.e.m.). Statistical significance was determined by calculating the proportion of the bootstrap difference distribution (Delta)

that crossed zero:

$$P = 2 \cdot \min\left(\frac{1}{N}\sum_{i=1}^{N}\mathbb{I}(\Delta_i \geq 0), \frac{1}{N}\sum_{i=1}^{N}\mathbb{I}(\Delta_i \leq 0)\right) \tag{21}$$

where N represents the total number of bootstrap iterations (10,000), Delta_i is the calculated difference at iteration i, and I(·) is an indicator function that equals 1 if the internal condition is true and 0 otherwise. Calculated P-values were lower-bounded at 1/N, yielding a minimum possible P-value of 0.0001.

Standard statistical tests and normality

For datasets where hierarchical nesting was not applicable, such as mouse-level behavioral parameters in Figure 1 and Figure 6, an automated analysis pipeline determined the most appropriate frequentist test. The normality of each group was evaluated using the Shapiro-Wilk test. For normally distributed data, parametric independent or paired t-tests were implemented, applying Welch's correction in cases of unequal variance between independent cohorts. When the assumption of normality was violated, non-parametric alternatives were used, specifically the Mann-Whitney-U test for independent samples and the Wilcoxon signed-rank test for paired designs.

Figures

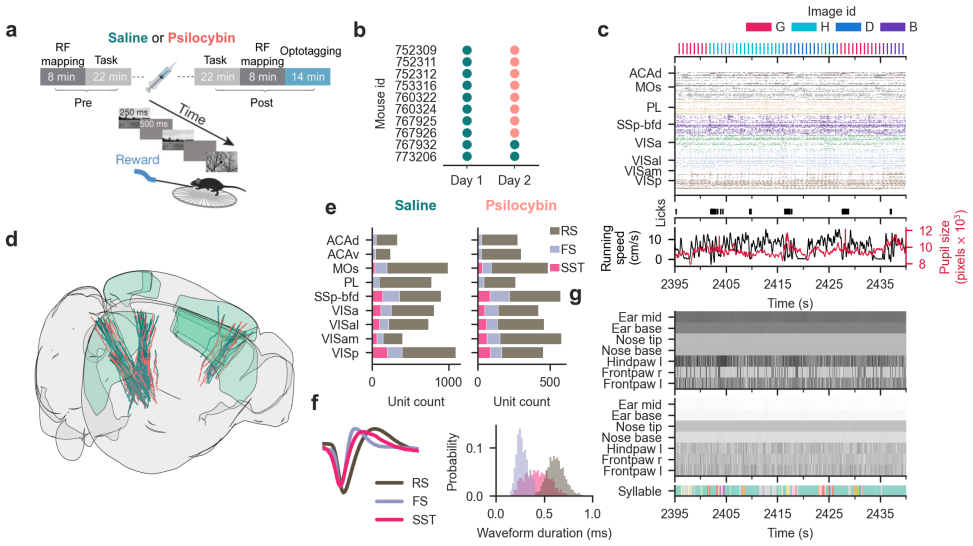

Fig. 1 Visual change-detection task and Neuropixels recordings in visual and frontal cortices.

(A) Change detection task and experimental design. In brief, head-fixed mice detected image changes in a series of image presentations (250ms with 500ms inter-stimulus interval) by licking a lick spout to collect water reward for correct responses. Receptive field (RF) mapping was conducted before and after task epochs, and opto-tagging of SST interneurons was conducted at the end of each recording session. The behavioral task period was split into a pre- and post-injection epoch, with either saline or psilocybin injections.

(B) Experimental design across mice and sessions comprising paired within-animal recording sessions (n=10 mice, n=12 saline and n=8 psilocybin sessions), plus two saline-only controls. Mouse 760322 was excluded from task performance analysis due to chance-level perceptual sensitivity across both sessions. The psilocybin session for mouse 752309 was excluded from task performance and neural analyses due to a data

synchronization failure.

(C) Forty-five seconds sample of simultaneously recorded behavioral and neural data (image presentations, spiking activity, licking, running speed, and pupil diameter). Anatomical abbreviations: ACAd, Anterior cingulate area dorsal; MOs, Secondary motor area; PL, Prelimbic area; SSp-bfd, Primary somatosensory area, barrel field; VISa, Anterior visual area; VISam, Anteromedial visual area; and VISp, Primary visual area.

(D) 3D rendering of all Neuropixels probes, n=71 for saline (teal) and n=48 for psilocybin (salmon) across visual and frontal cortices.

(E) A total of 11,012 recorded single-units broken down for cortical area, saline (teal, left) and psilocybin (salmon, right).

(F) Left: Average waveform per neuron type. Right: Waveform duration distribution per neuron type, grey for RS, blue for FS and pink for SST.

(G) Spatial coordinates (top, medio-lateral axis; middle, ventro–dorsal axis) of seven body-features tracked from the frontal video. On the bottom, quantification of whole-body motor kinematics using MoSeq to identify motor syllables.

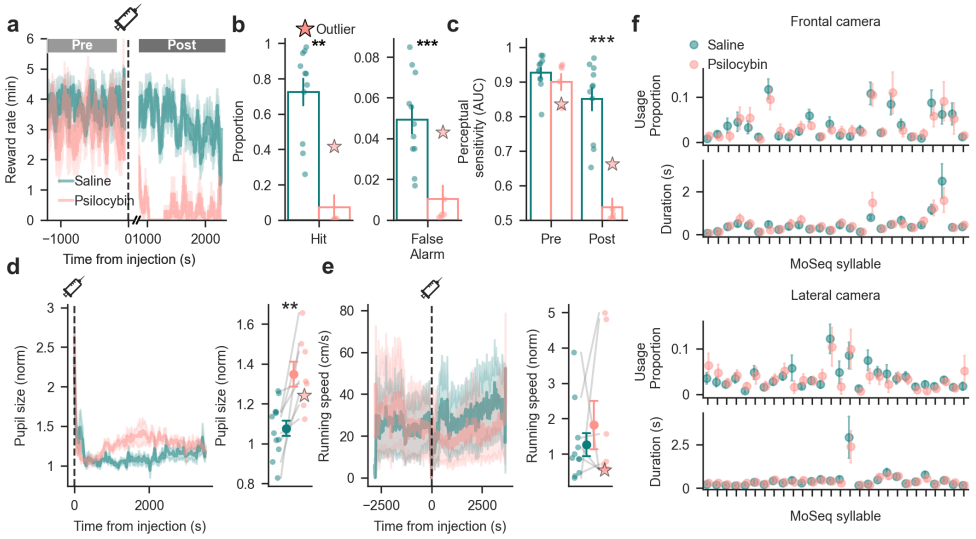

Fig. 2 Psilocybin impairs performance in a change detection task.

(A) Psilocybin abruptly and significantly impaired change detection performance relative to saline controls. Shading indicates ±1 s.e.m.

(B) Hit and false alarm rate in the post-injection epoch. Performance deficits were driven by reductions in both hit and false alarm rates. Individual points represent single behavioral sessions (n = 11 saline, n = 6 psilocybin). Error bars correspond to ±1 s.e.m.

(C) Perceptual sensitivity (AUC) collapsed to chance levels in the post-injection epoch under psilocybin. Individual points represent single behavioral sessions (n = 11 saline, n = 6 psilocybin). Error bars correspond to ±1 s.e.m.

(D) Psilocybin induced a significant increase in pupil diameter. Within each session, pupil diameter was normalized by dividing it by the mean pupil diameter during the pre-injection baseline period.. Shading indicates ±1 s.e.m. Individual points represent single behavioral sessions (n = 12 saline, n = 8 psilocybin).

(E) Running speed was unaffected by psilocybin administration. Shading indicates

±1 s.e.m. Individual points represent single behavioral sessions (n = 11 saline, n = 8 psilocybin); running data was unavailable for one session.

(F) Motor kinematics (syllable usage proportion and duration) derived from the frontal (top) and lateral (bottom) camera showed no significant differences between conditions (Kruskal-Wallis test, $p>0.05$ for all syllables). Error bars correspond to ±1 s.e.m. *$P < 0.05$, ***$P < 0.01$, ***$P < 0.001$.

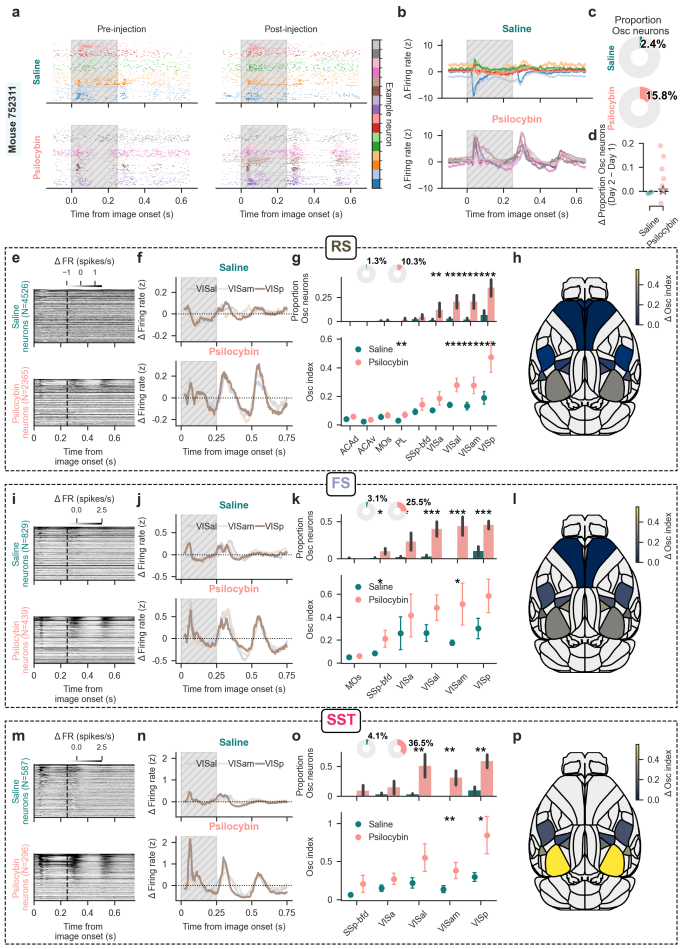

Fig. 3 Psilocybin induces an oscillatory modulation strongest in SST interneurons.

(A) Example raster plot of 8 representative neurons before (top) and after (bottom) injection of saline (left) or psilocybin (right). The hatched gray area indicates the duration of image presentation.

(B) PSTHs of the difference between post- and pre-injection epochs. Each line represents one neuron; neurons from (A) are color-coded accordingly. The hatched gray area indicates the duration of image presentation.

(C) Fraction of cortical neurons classified as Osc neurons after injection of saline (top) or psilocybin (bottom).

(D) Increase in Osc neurons between experimental sessions. Points represent individual animals.

(E) Heatmaps of the change in firing rate (Δ Firing rate = post - pre) for RS neurons, sorted by the Osc index. Data are shown for saline (top) and psilocybin (bottom) groups, aligned to image onset. The dashed line indicates the end of image presentation.

(F) Average ΔFiring rate traces for VISp, VISam, and VISal, the areas exhibiting the strongest modulation following psilocybin. The hatched gray area indicates the duration of image presentation.

(G) Top, fraction of Osc neurons in each cortical area. P: ACAd, 1.0; ACAv, 1.0; MOs, 1.0; PL, 0.65; SSp-bfd, 0.24; VISa, 0.010; VISal, 0.001; VISam, 0.001; VISp, 0.001, hierarchical bootstrap; pie charts indicate the total percentage of Osc neurons per group. Bottom, distribution of mean Osc index across areas. P: ACAd, 0.090; ACAv, 0.10; MOs, 0.29; PL, 0.002; SSp-bfd, 0.17; VISa, 0.068; VISal, 0.001; VISam, 0.001; VISp, 0.001, hierarchical bootstrap. Error bars correspond to ± 1 s.e.m.

(H) Brain map showing the difference in mean Osc index between psilocybin and saline sessions.

(I)-(L) Same as E-H for FS neurons. In (K), top P: MOs, 0.55; SSp-bfd, 0.030; VISa, 0.56; VISal, 0.10; VISam, 0.012; VISp, 0.068, hierarchical bootstrap. Bottom, P: MOs, 1.0; SSp-bfd, 0.032; VISa, 0.046; VISal, 0.001; VISam, 0.001; VISp, 0.001, hierarchical bootstrap.

(M)-(P) Same as E-H for SST neurons. In (O), top P: SSp-bfd, 0.20; VISa, 0.17; VISal, 0.10; VISam, 0.004; VISp, 0.016, hierarchical bootstrap. Bottom, P: SSp-bfd, 0.64; VISa, 0.25; VISal, 0.006; VISam, 0.002; VISp, 0.002, hierarchical bootstrap. $^{*}P < 0.05$, $^{***}P < 0.01$, $^{***}P < 0.001$.

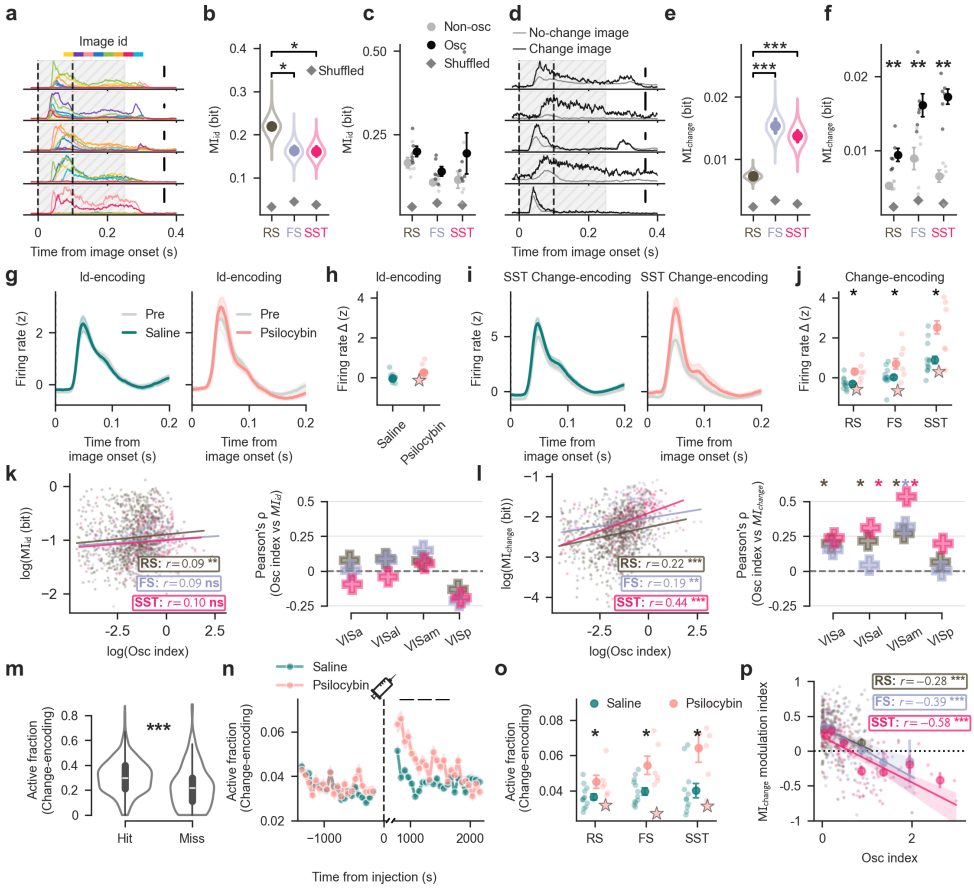

Fig. 4 Psilocybin preferentially modulates change-encoding neurons.

(A) Five representative single-units encoding image id from one session. Vertical dashed lines indicate the 0–100 ms window used to compute MI. The hatched gray area indicates the duration of image presentation. Scale bar 40 spikes/s.

(B) Distribution of MIid values across neuron types (right), with 3 bits necessary to encode image id. RS neurons exhibit an enrichment in MIid (RS = 0.220 ± 0.004 bits versus FS = 0.163 ± 0.005 versus SST = 0.162 ± 0.005; mean ± s.e.m.; P = 0.048 for RS vs FS, P = 0.042 for RS vs SST; hierarchical bootstrap nested by session and brain area).

(C) No significant differences in MId in Osc neurons (Mann-Whitney U test, P=RS: 0.13, FS: 0.24, SST: 0.31). Error bars correspond to ±1 s.e.m.

(D) Five representative single-units encoding image change from the same session as in A.

(E) Distribution of MIchange values across SST-inhibition based categories (left) and neuron types (right), with 1 bit necessary to encode an image change. FS and SST neurons exhibit an enrichment in MIchange (RS = 0.0074 ± 0.0001 bits versus FS = 0.0154 ± 0.0006 versus SST = 0.0138 ± 0.0005; mean ± s.e.m.; P <0.001 for RS vs FS, P <0.001 for RS vs SST, hierarchical bootstrap nested by session and brain area).

(F) MIchange is enriched in psilocybin modulated cells across neuron types (Mann-Whitney U test, P=RS: 0.002, FS: 0.004, SST: 0.002). Psilocybin-modulated cells are defined as the ones with an Osc index in the top 20% percentile. Error bars correspond to ±1 s.e.m.

(G) Firing rate of image id-encoding neurons during no-change trials pre-injection (gray) and post-injection (left: saline, teal; right: psilocybin, salmon).

(H) Change in firing rate induced by saline or psilocybin injection, quantified in a 10 ms window centered at the peak response.

(I) Firing rate of SST change-encoding neurons during no-change trials pre-injection (gray) and post-injection (left: saline, teal; right: psilocybin, salmon).

(J) Change in firing rate induced by saline or psilocybin injection across neuron types, quantified in a 10 ms window centered at the peak response. All neuron types exhibited a significant difference.

(K) Correlation between Osc index and MId. Left: Pearson correlation pooled across areas. Only RS neurons showed a significant, weak positive correlation (RS: r = 0.09, P = 0.007). Right: Within-area correlation. No region-cell type pair survived FDR correction (P >0.05, two-sided permutation test).

(L) Correlation between Osc index and MIchange. Left: Pearson correlation pooled

across areas. All cell types showed significant positive correlations, strongest in SST neurons (RS: r = 0.22; FS: r = 0.18; SST: r = 0.44; all P <0.005). Right: Within-area correlation. Positive correlations survived FDR correction (P <0.05, two-sided permutation test) for all cell types in VISam, RS in VISa, and RS/SST in VISal.

(M) The active fraction of change-encoding neurons during change trials was significantly higher for hits than for misses during pre-injection.

(N) Time course of the active fraction of change-encoding neurons during no-change images before and after injection. Psilocybin temporarily increases the active fraction. Grey rectangles represent significance calculated on 5-minute windows (window 1: P=0.022; window 2: P=0.035; window 3: P=0.043; independent t-test).

(O) Average active fraction in the 30 min post-injection, shown by neuron type. The star ($\star$) denotes the behavioral outlier. Each dot represents one session.

(P) Pearson correlation between the MIchange modulation index, quantifying discriminability across epochs of no-change responses compared to pre-injection change responses, and Osc index across change-encoding neurons in psilocybin sessions, shown separately for each neuron type. $^{*}P < 0.05$, $^{***}P < 0.01$, $^{***}P < 0.001$.

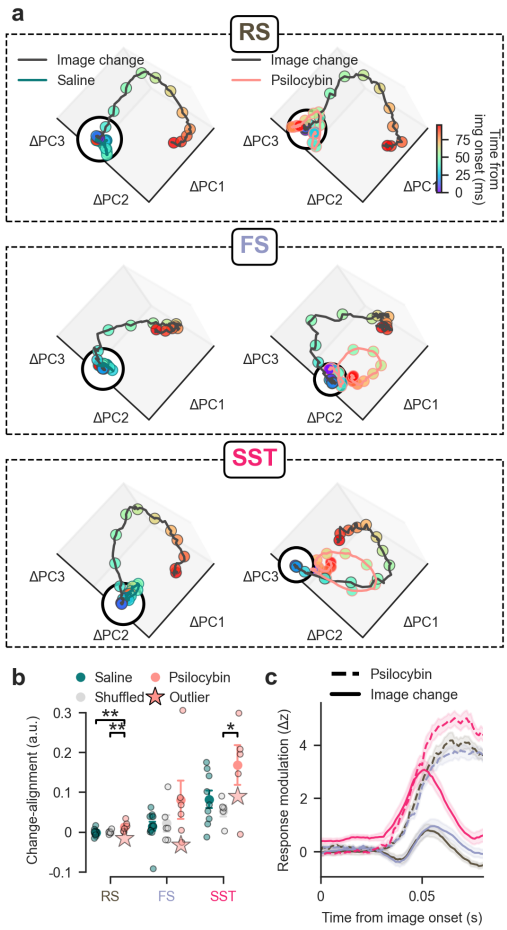

Fig. 5 Psilocybin shifts population dynamics in visual cortex towards change-like states

(A) Population trajectory shifts induced by image changes (black line) or injections of saline (teal, left) or psilocybin (salmon, right), projected into a common neural state space. Shifts are calculated relative to baseline activity during pre-injection no-change trials. Dots are color-coded by post-stimulus time (0-100 ms). Rows correspond to neuron types; the black circle denotes the origin.

(B) Scalar projection of the injection-effect vector onto the change-effect vector across sessions (see text for details). Psilocybin increases trajectory alignment with genuine image changes in RS and SST neurons, whereas saline and shuffled controls do not.

The star ($\star$) denotes the behavioral outlier. Each dot represents one session. Error bars correspond to ± 1 s.e.m. $^{*}P < 0.05$, $^{***}P < 0.01$, $^{***}P < 0.001$.

(C) Response kinetics of the pre-injection image-change response (Image change, solid lines) and the post-psilocybin no-change response (Psilocybin, dashed lines) in change-encoding neurons, aligned to image onset. Pre-injection no-change responses were subtracted from both conditions to isolate baseline-independent dynamics. Cell types are color-coded as in B. Shading indicates ± 1 s.e.m.

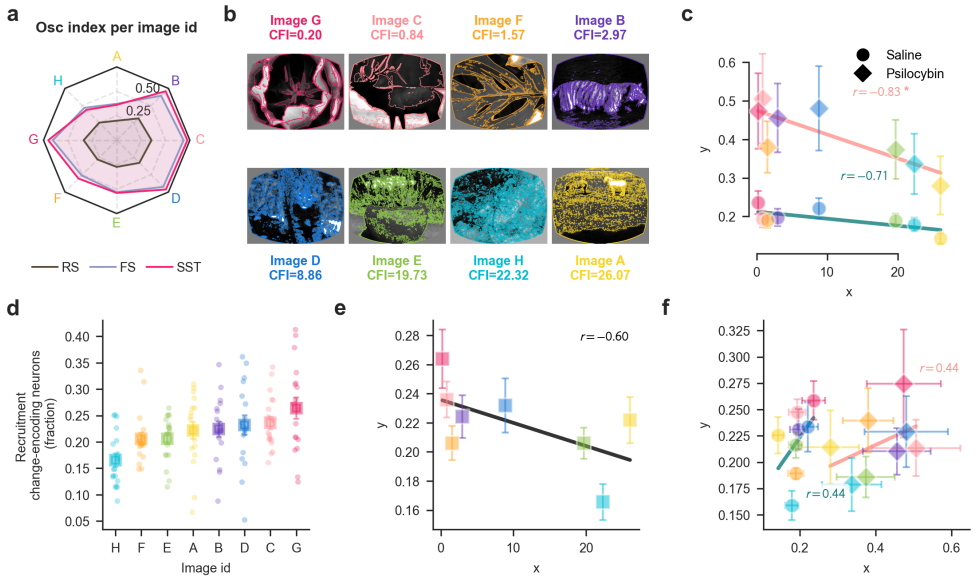

Fig. 6 Stimulus features determine the magnitude of psilocybin-induced modulation

(A) Magnitude of psilocybin-induced modulation shown separately for each image A through H in the stimulus set.

(B) The eight natural images used in the task. Colored overlays indicate detected contours used to compute the Contour Fragmentation Index (CFI).

(C) Correlation between CFI and Osc index across images in psilocybin (diamonds) and saline (circles) sessions.

(D) Recruitment of change-encoding neurons following genuine image changes across all sessions, shown separately for each image.

(E) Relationship between CFI and recruitment of change-encoding neurons across images across all sessions.

(F) Relationship between Osc index and recruitment of change-encoding neurons across images in psilocybin (diamonds) and saline (circles) sessions.

Error bars correspond to ±1 s.e.m.

Supplementary information.

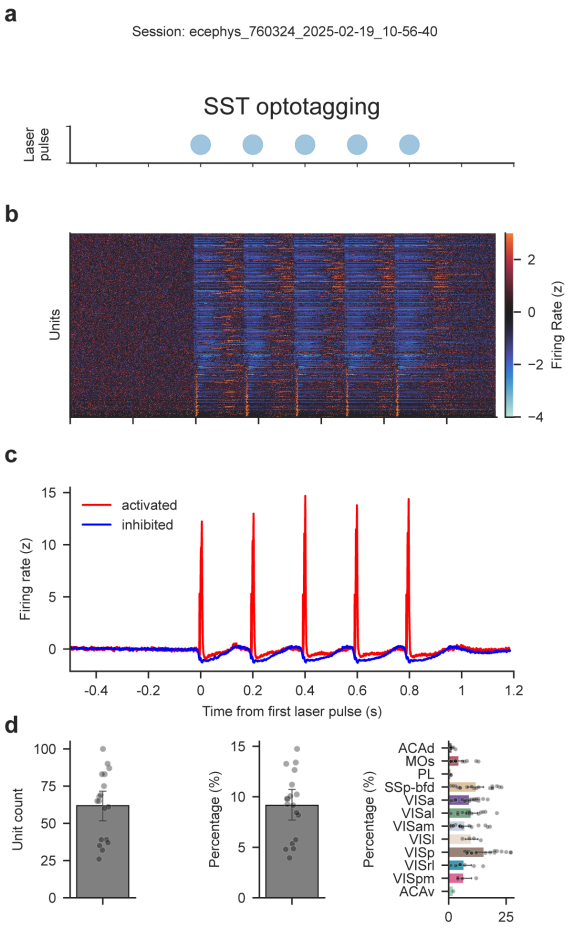

Fig. S1 Optotagging identifies SST interneurons

(a) 5 Hz laser pulse.

(b) Single-unit fZz-scored firing rates of an example session (ecephys-760324-2025-02-19-10-56-40) aligned to laser pulses shown in a during the optotagging protocol. Shown here are Here visible all the neurons with significantly modulation following laser stimulationed.

(c) Average firing rate of activated and inhibited neurons in of the same session as (b).

(d) Average count (left) and percentage (center) of optotagged cortical neurons per session. Right: average percentage of optotagged neurons per cortical area.

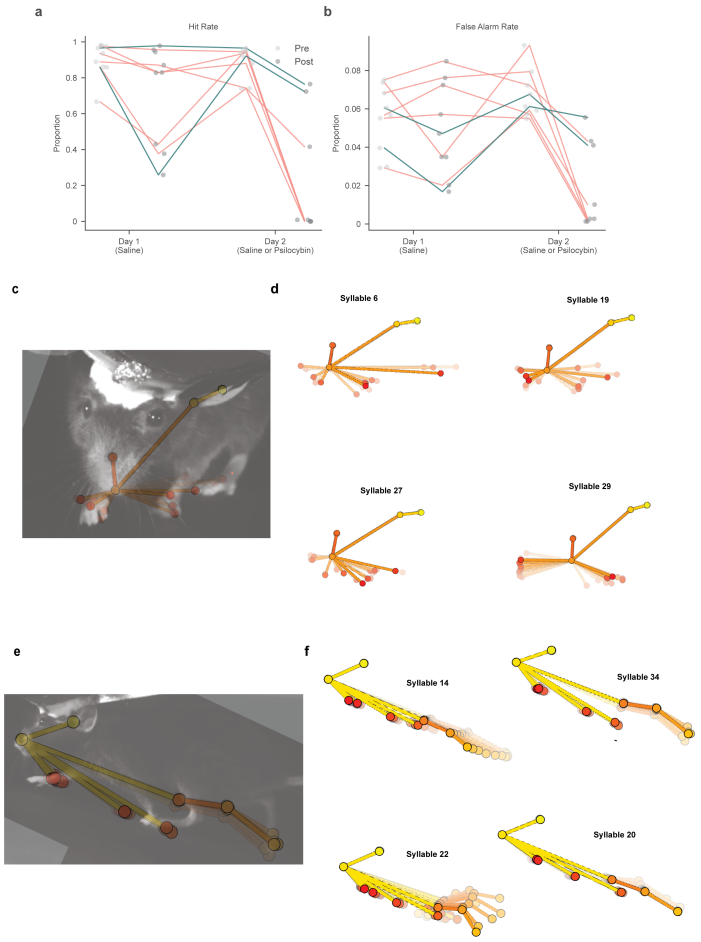

Fig. S2 Behavioral performance and MoSeq analysis

(a) Hit rate measured before (Pre, light gray circles) and after (Post, dark gray circles) injection across Day 1 and Day 2. Each circle represents a single behavioral session. Lines connect the performance trajectories of individual animals across experimental epochs and days. Teal lines track control animals that received saline injections on both days (n = 2).

(b) False alarm rate across experimental epochs and days, formatted identically to (a).

(c) Frontal camera view with superimposed keypoints extracted with DeepLabCut.

(d) Example syllables extracted from frontal camera videos. Each trajectory plot shows

a sequence of poses along the average trajectory through latent space associated with a given syllable.

(e) Same as (c) for lateral camera videos.

(f) Same as (d) for lateral camera videos.

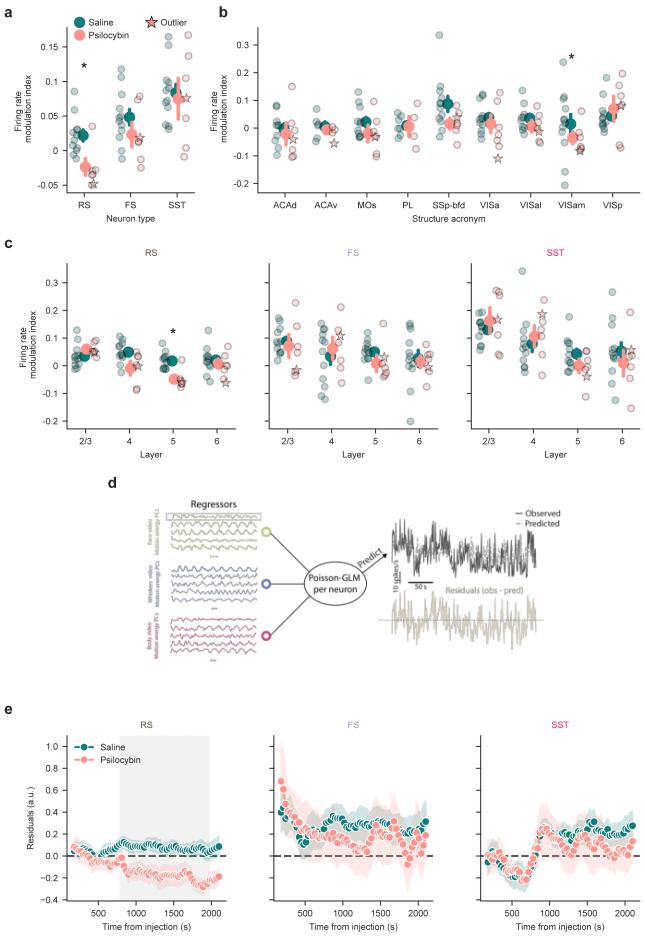

Fig. S3 Psilocybin decreases activity in cortical RS neurons

(a) Firing rate modulation index across neuron types. Psilocybin causes a significantsignificance decrease of in firing rates in RS neurons (psilocybin = -0.024 ± 0.012, saline = 0.022 ± 0.008, mean ± s.e.m. across sessions, p = 0.0478, hierarchical bootstrap).

(b) Firing rate modulation index across brain areas, with. nNO sdignificant differences.

(c) Firing rate modulation index across layers and neuron types. Psilocybin causes a significantsignificance decrease ofin firing rates in layer 5 RS neurons (psilocybin =

-0.048 ± 0.014, saline = 0.017 ± 0.008, mean ± s.e.m. across sessions, p = 0.019, hierarchical bootstrap).

(d) Schematic of the GLM-based prediction. We extracted 40 principal components (PCs) from three behavioral videos using FaceMap. These PCs were used as regressors in a Poisson GLM fitted to each neuron's activity during the pre-injection block. The model was then used to predict firing rates in the post-injection block. Residuals were computed as (observed - predicted) / √(predicted), yielding standardized residuals.

(e) Grand average time course of residuals per group (psilocybin vs. saline). Residuals were first aggregated within each session using a median estimator (see Methods). RS neurons exhibit a significant decrease in firing rate beginning ~30 min post-injection. Gray rectangle represents p <0.05 using Mann-Whitney-U u test. Shading indicates ±1 s.e.m. Error bars in all panels represent ±1 s.e.m.

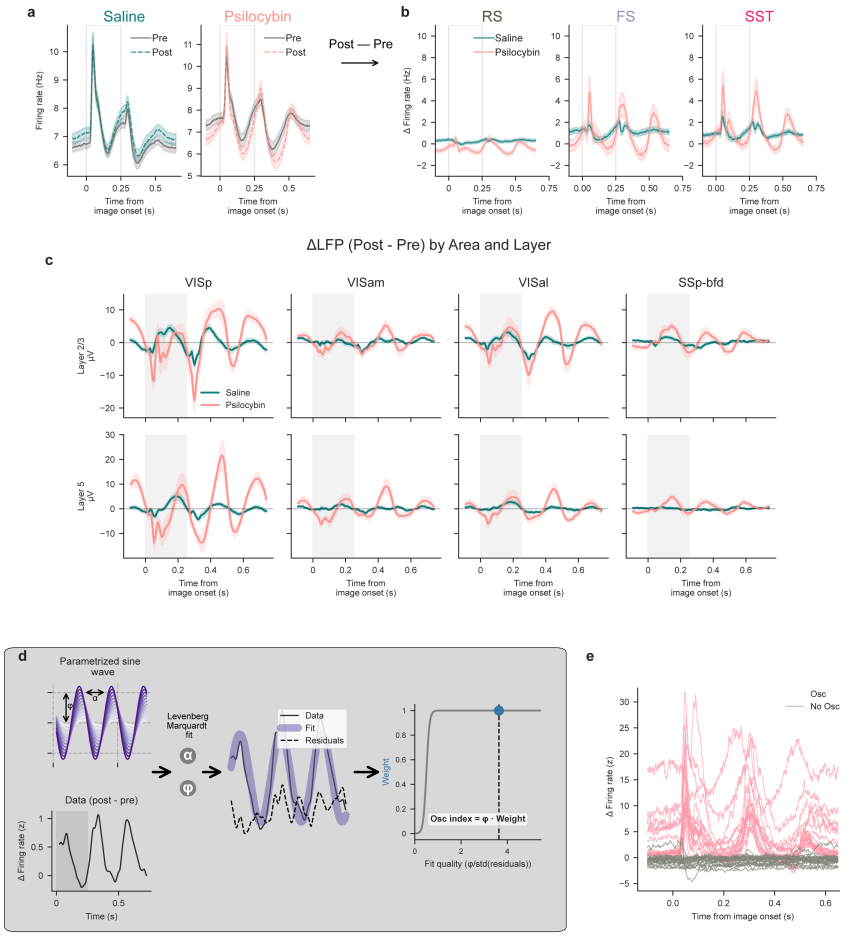

Fig. S4 Psilocybin induces a a 4-Hz oscillation in visual cortex across scales

(a) Average PSTH of all cortical neurons aligned to all non-change images pre and post injection. Psilocybin causes a rhythmic change in firing rate. Shading indicates ± 1 s.e.m.

(b) ΔPSTH (post - pre epochs) of all cortical neurons recorded separately for each divided by cell type. A clear modulation is visible across cell types, prominently in FS and SST neurons. Shading indicates ± 1 s.e.m.

(c) Layer 2/3 (top row) and layer 5 (bottom row) delta LFPs of VISp, VISam, VISal and SSp-bfd. Each delta LFP is computed by subtracting the image onset-aligned

(only non-change)traces of the pre- injection block from the post-injection block. The psilocybin group shows a clear modulation similar to the one shown in the spike analysis. Shading indicates ± 1 s.e.m.

(d) Analytical framework for calculating the oscillation index computation. A 4- Hz sine wave was fitted to the delta PSTH (post-injection minus pre-injection epochs) of each individual neuron by optimizing both amplitude and phase. The resulting residuals were used to calculate a fit-quality metric, defined as the ratio of the fitted amplitude to the standard deviation of the residuals. To ensure the index selectively reflects robust rhythmic activity, the final oscillation index was down-weighted in cases of low fit quality (see Methods).

(e) Example neurons from session ecephys_752311_2025-01-23_14-00-04. Osc index can reliably identify strongly highly oscillating modulated neurons.

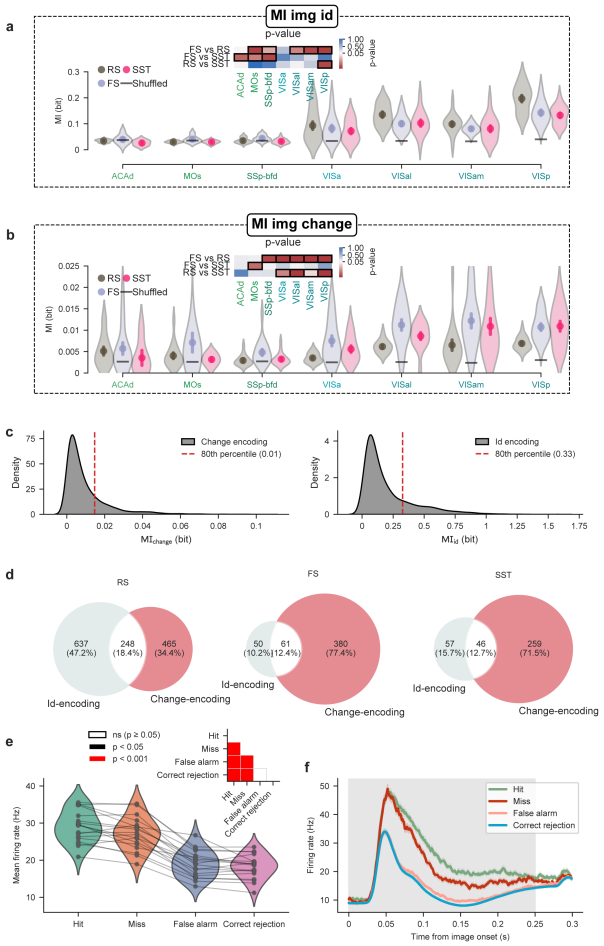

Fig. S5 Encoding of image id and change across cortical neurons.

(a) MIid enrichment across visual areas and neuron types. Inset matrix shows p-values for each comparison; red indicates p <0.05, with darker shades representing stronger significance, while blue-to-white transitions denote values approaching significance (hierarchical bootstrap accounting for session id).

(b) MIchange enrichment in FS and SST neurons is significant across visual areas. Inset matrix shows p-values for each comparison; red indicates p <0.05, with darker shades representing stronger significance, while blue-to-white transitions denote values approaching significance (hierarchical bootstrap accounting for session id).

(c) Distribution of MIchange (left) and MIid (right) values across neuron types.

(d) Venn diagrams showing the overlap between change- and id-encoding neurons across neuron types.

(e) Mean firing rate of change-encoding neurons across trial types (cCorrect rejection = 10.82 ± 0.34 spikes/s versus fFalse alarm = 11.325 ± 0.327 spikes/s versus hHit = 14.659 ± 0.44 spikes/s versus mMiss = 13.67 ± 0.546 spikes/s; mean ± s.e.m.; p- values determined by pairwise Wilcoxon signed-rank tests with Bonferroni correction). Inset shows the p-value significance matrix.

(f) PSTHs of change-encoding neurons stratified by trial type.

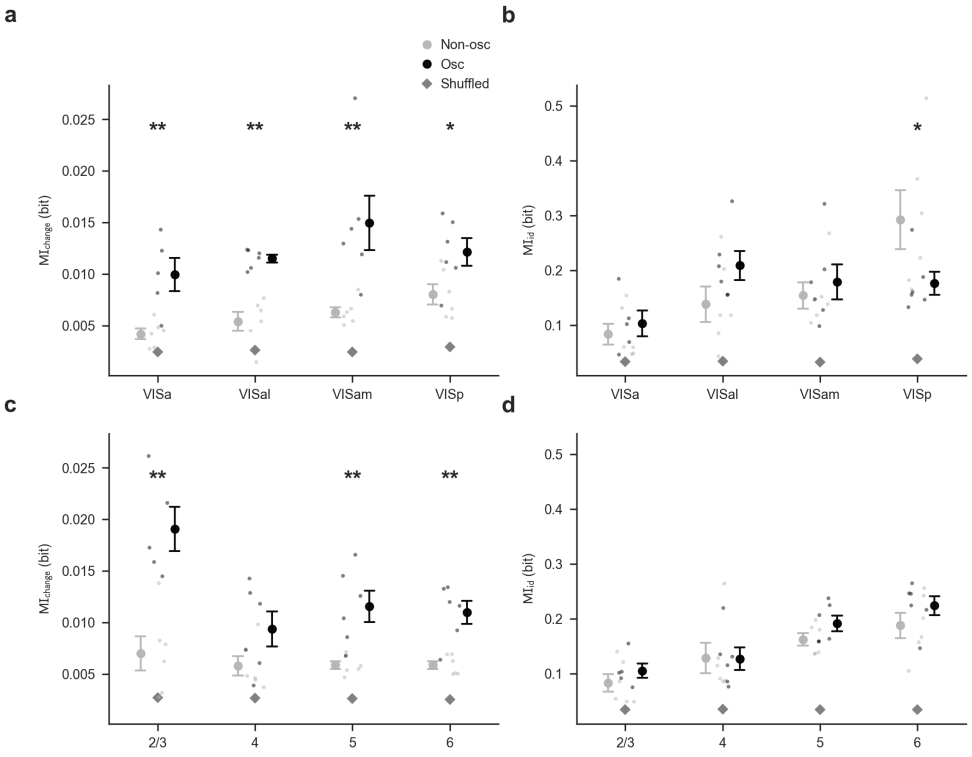

Fig. S6 Change information is preferentially enriched in psilocybin-modulated cells across visual areas and cortical layers

(a) MIchange is enriched in psilocybin- modulated cells across brain areas (p: VISa, p=0.039, VISal, p<0.001, VISam, p<0.001, VISp, p=0.016, hierarchical bootstrap). Psilocybin-modulated neurons cells are defined as neuronsthe ones with an Osc index in the top 20% percentile. (b) No widespread differences in MIid by brain area, with the exception of VISp showing significantly reduced MIid in psilocybin-modulated cells (p: VISa, p=0.9327, VISal, p=0.5435, VISam, p=0.302, VISp, p=0.017, hierarchical bootstrap).(c) Bottom: MIchange is enriched in psilocybin- modulated neurons cells across cortical layers, with layer 2/3 being particularly enriched, while layer 4 showings no enrichment (p: 2/3, p<0.001;, 4, p=0.144;, 5, p<0.001;, 6, p<0.001, hierarchical bootstrap).(d) Bottom: No significant differences in MIid across by cortical layers,

with, except within layer 5 showing an enrichment in Osc neurons (p: 2/3, p=0.3769;, 4, p=0.989;, 5, p<0.001;, 6, p=0.4547, hierarchical bootstrap).

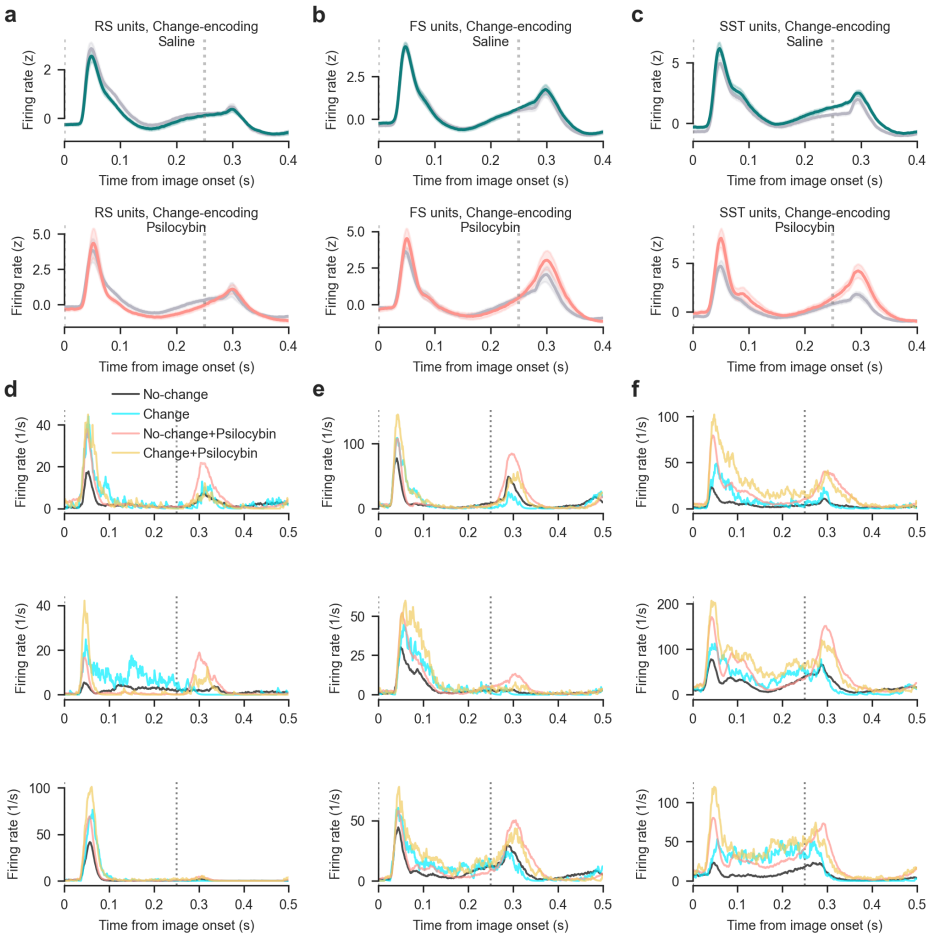

Fig. S7 Change-encoding neurons' responses across experimental conditions

(a) Top: responses of RS change-encoding neurons to no-change images before and after saline injection. Bottom: responses of RS change-encoding neurons to no-change images before and after psilocybin injection.

(b) Same as (a) for FS change-encoding neurons.

(c) Same as (a) for SST change-encoding neurons.

(d) Responses of three single RS neurons to no-change (both before and after psilocybin injection) and change images.

(d) Responses of three single FS neurons to no-change (both before and after psilocybin injection) and change images.

(d) Responses of three single SST neurons to no-change (both before and after psilocybin injection) and change images.

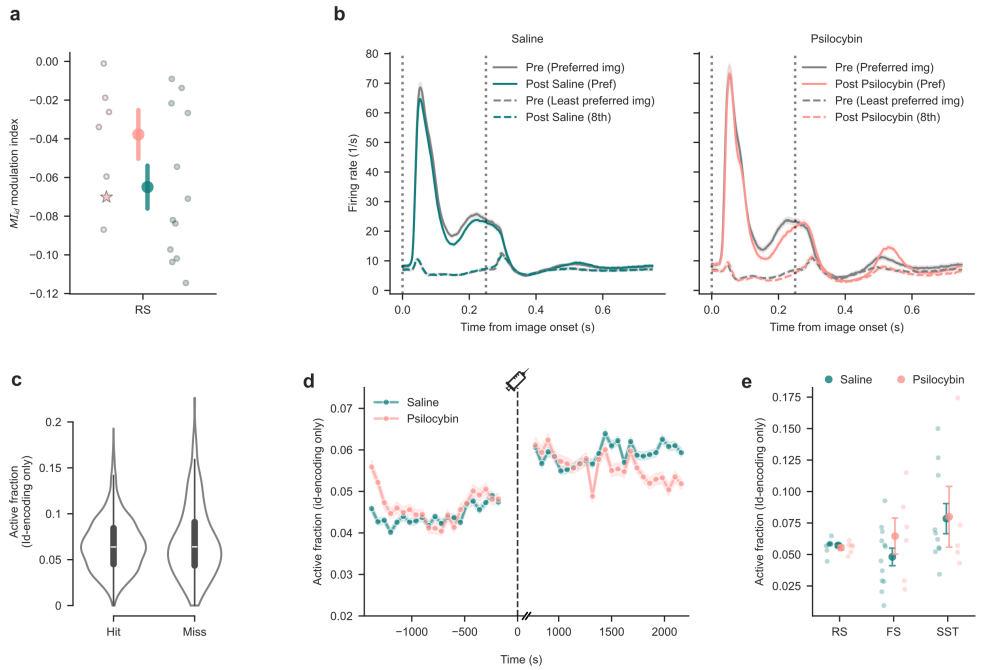

Fig. S8 Image id-encoding neurons are not affected by psilocybin.

(a) Change in Average MIid in image identity-encoding neurons after injection, showing no significant change between saline and psilocybin conditions.

(b) Population PSTHs of image identity-encoding neurons to their preferred (rank 1) and least preferred (rank 8) image before and after injection of saline (left) or psilocybin (right).

(c) Active fraction of image id-encoding neurons during change trials is not different between hit and miss trials.

(d) Active fraction of image id-encoding neurons across before and after saline or psilocybin injection, showing no No effect of psilocybin on image id-encoding neurons time course of active fraction before and after injection.

(e) Active fraction is not different between groups in all three neuron types.

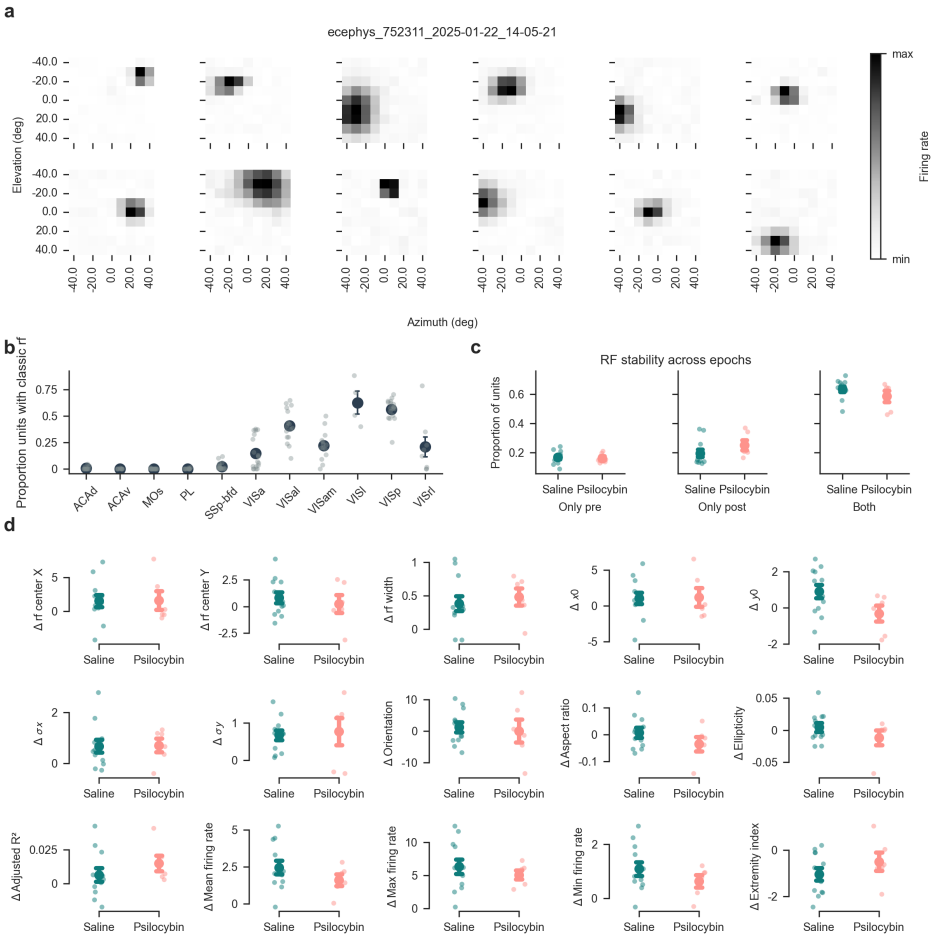

Fig. S9 Receptive field tuning is not affected by psilocybin

(a) Representative examples of neurons with classic receptive field (RF) tuning. (b) Proportion of neurons per brain area exhibiting classical RF responses per brain area.

(c) Proportion of neurons showing RF tuning only before injection (pre), only after injection (post) or in both epochs. Psilocybin does not affect the RF stability.

(d) Psilocybin-evoked changes in RF parameters, compared to saline. Each panel shows the per-session mean change (δ = post - pre) for a given spatial, geometric, or baseline response metric. Extracted features encompass empirical properties (RF

center x (define axis), RF center y (define axis), and RF width), parametric variables optimized via rotated 2d Gaussian surface fits (x_0, y_0, σ x, σ y, oOrientation, aAspect ratio, eEllipticity, and aAdjusted R^2), and global non-parametric matrix dynamics (eExtremity index, mMean firing rate, mMin firing rate, and mMax firing rate). Each individual dot represents a single session average, and the point plots display the group mean ± s.e.m. No significant differences in parameter dynamics were observed between the psilocybin and saline experimental cohorts (hierarchical bootstrap, all uncorrected $p > 0.05$).

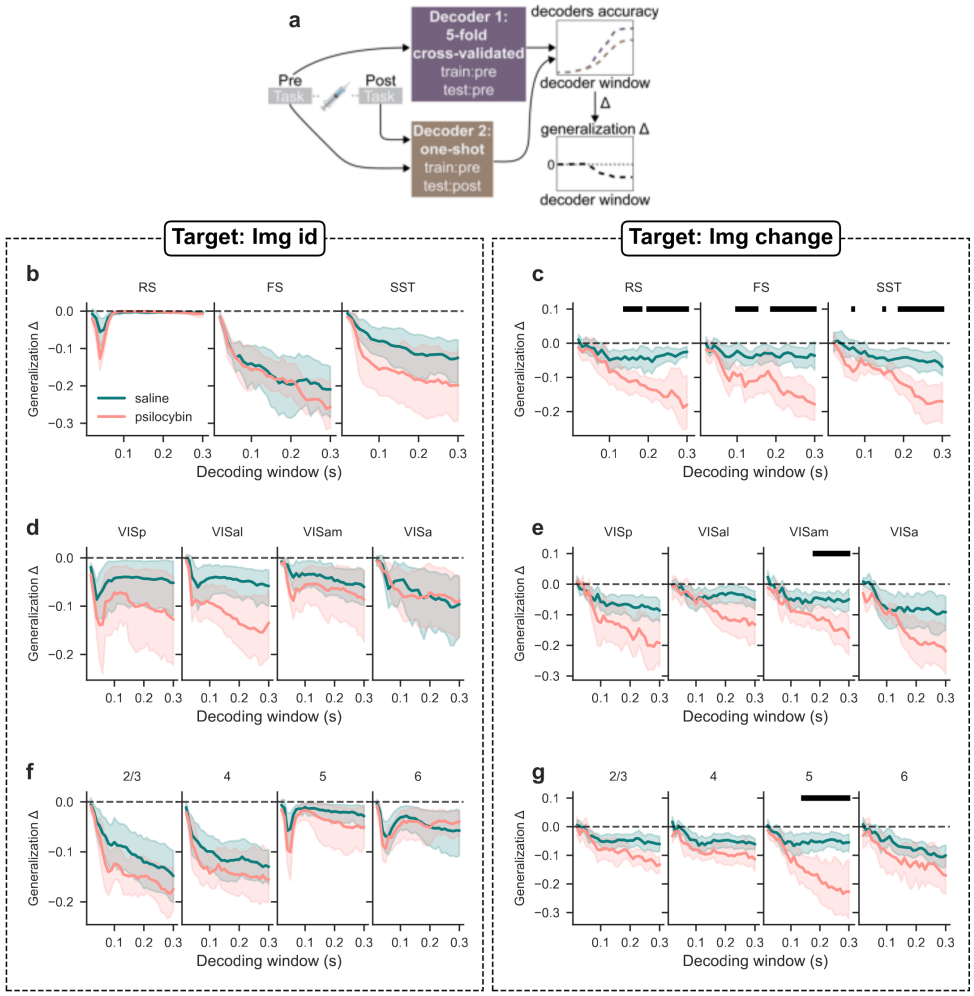

Fig. S10 Decoding image identity and change across neuron types, brain areas and cortical layers.

1. Decoding procedure schematic.

(b) Decoding accuracy for image identity over increasingly large time windows across functional neuron types. Black horizontal bars indicate significant differences between injection conditions ($p < 0.05$, FDR-corrected independent two-sample t-tests).

(c) Decoding accuracy for image change over increasingly large time windows across functional neuron types.

(d) Decoding accuracy for image identity over increasingly large time windows across distinct brain areas.

(e) Decoding accuracy for image change over increasingly large time windows across distinct brain areas.

(f) Decoding accuracy for image identity over increasingly large time windows across cortical layers.

(g) Decoding accuracy for image change over increasingly large time windows across cortical layers.

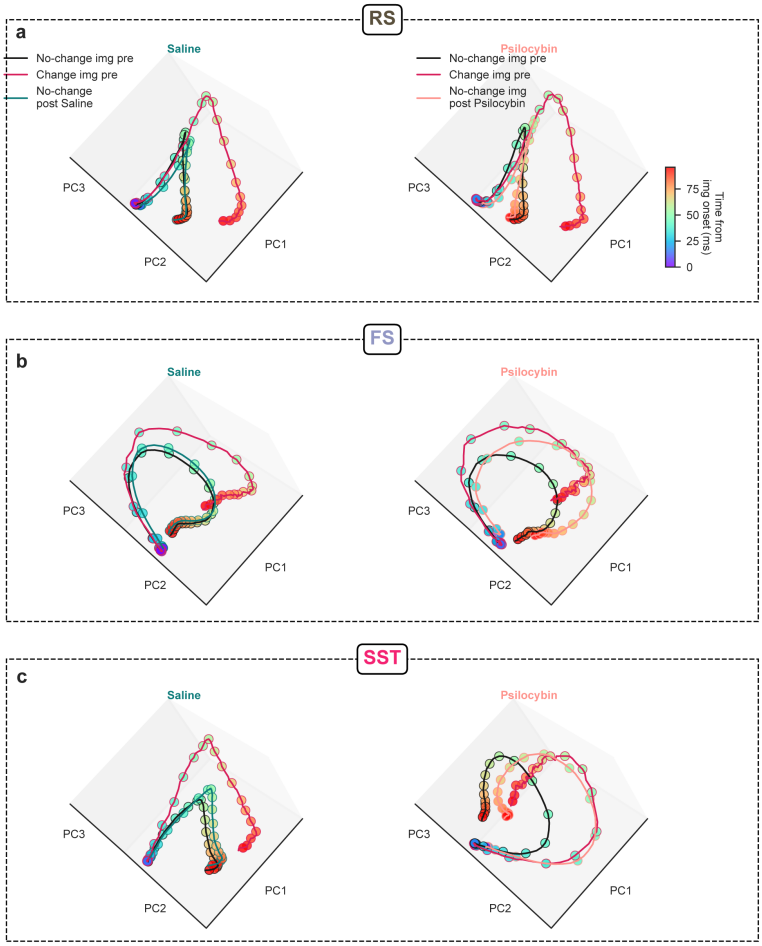

Fig. S11 Psilocybin shifts sensory representation of non-change images in SST neurons

(a) RS-neuron population trajectory in the space defined by the first three principal components (PCs), showing RS Population activity of RS neurons in PCA-defined subspace PCA trajectories of RS neurons activity during no-change images (black line), change images (orange line) and no-change images after injection (saline in teal on the left column, psilocybin in salmon on right column). Superimposed dots represent time progress from image onset 0-100 ms (white to black).

(b) Same as (a) for FS neurons.

(c) Same as (a) for SST neurons.

Contribution Matrix

Acknowledgments. This work was supported by the European Research Council (ERC) under the European Union's Horizon Europe research and innovation programme [grant agreement number 101117587, TIMEVALUE (TO)]. The experimental Neuropixels dataset in this project was obtained as part of the OpenScope program, which is operated by the Allen Institute, Neural Dynamics program and funded by the US National Institutes of Health (NIH) [grant numbers: U24NS113646 (JAL, CK)]. We thank the OpenScope steering committee and Karel Svoboda for their support. This research was also supported by the Allen Institute, founded by Jody Allen – chair and co-founder of Allen Family Philanthropies, and the late Paul G. Allen – investor, philanthropist, and co-founder of Microsoft. We gratefully acknowledge their vision and generosity, which make this work possible. We thank Willy Schiegel for technical help with cluster computing. We thank members of Ott lab, Dennis Nestvogel

and Loreen Hertäg for discussion. The authors declare that they have no competing interests.

Declarations

Availability of data and materials

All the code used to process the dataset is available at https://github.com/RobertoDF/psycode. All figures and text can be reproduced using code present in this repository. Access to the original datasets is provided on the Dandi platform https://dandiarchive.org/dandiset/001417.

Competing interests

CK holds an executive position, and has a financial interest, in Intrinsic Powers, Inc., a company whose purpose is to develop a device that can be used in the clinic to assess the presence of consciousness in patients.

References

[1] Key, B. J. Effects of Chlorpromazine and Lysergic Acid Diethylamide on the Rate of Habituation of the Arousal Response. *Nature* **190**, 275–277 (1961). URL https://doi.org/10.1038/190275a0.

[2] Terrill, J. The nature of the LSD experience. *The Journal of nervous and mental disease* **135**, 425–9 (1962).

[3] Kometer, M. & Vollenweider, F. X. *Serotonergic Hallucinogen-Induced Visual Perceptual Alterations*, 257–282 (Springer Berlin Heidelberg, Berlin, Heidelberg, 2018). URL https://doi.org/10.1007/7854_2016_461.

[4] Carhart-Harris, R. L. & Friston, K. J. Rebus and the Anarchic Brain: Toward a Unified Model of the Brain Action of Psychedelics. *Pharmacol Rev* **71**, 316–344 (2019). 1521-0081 Carhart-Harris, R L Friston, K J Wellcome Trust/United Kingdom Journal Article Review Research Support, Non-U.S. Gov't United States Pharmacol Rev. 2019 Jul;71(3):316-344. doi: 10.1124/pr.118.017160.

[5] Corlett, P. R. *et al.* Hallucinations and Strong Priors. *Trends in Cognitive Sciences* **23**, 114–127 (2019). URL https://doi.org/10.1016/j.tics.2018.12.001. Doi: 10.1016/j.tics.2018.12.001.

[6] De Filippo, R. & Schmitz, D. Synthetic Surprise as the Foundation of the Psychedelic Experience. *Neuroscience & Biobehavioral Reviews* 105538 (2024). URL https://www.sciencedirect.com/science/article/pii/S014976342400006X.

[7] Siegle, J. H. *et al.* Survey of spiking in the mouse visual system reveals functional hierarchy. *Nature* **592**, 86–92 (2021). URL https://doi.org/10.1038/s41586-020-03171-x.

[8] Groblewski, P. A. *et al.* Characterization of Learning, Motivation, and Visual Perception in Five Transgenic Mouse Lines Expressing GCaMP in Distinct Cell Populations. *Frontiers in Behavioral Neuroscience* **Volume 14 - 2020** (2020). URL https://www.frontiersin.org/journals/behavioral-neuroscience/articles/10.3389/fnbeh.2020.00104.

[9] Attinger, A., Wang, B. & Keller, G. B. Visuomotor coupling shapes the functional development of mouse visual cortex. *Cell* **169**, 1291–1302. e14 (2017).

[10] Green, J. *et al.* A cell-type-specific error-correction signal in the posterior parietal cortex. *Nature* **620**, 366–373 (2023). URL https://doi.org/10.1038/s41586-023-06357-1.

[11] Keller, A. J., Roth, M. M. & Scanziani, M. Feedback generates a second receptive field in neurons of the visual cortex. *Nature* **582**, 545–549 (2020). URL https://doi.org/10.1038/s41586-020-2319-4.

[12] Adesnik, H., Bruns, W., Taniguchi, H., Huang, Z. J. & Scanziani, M. A neural circuit for spatial summation in visual cortex. *Nature* **490**, 226–231 (2012). URL https://pubmed.ncbi.nlm.nih.gov/23060193%0D%0Ahttps://www.ncbi.nlm.nih.gov/pmc/articles/PMC3621107/. 23060193[pmid] PMC3621107[pmcid] nature11526[PII].

[13] Bennett, C. *et al.* Map of spiking activity underlying change detection in the mouse visual system. *bioRxiv* 2025.10.17.683190 (2025). URL https://www.biorxiv.org/content/biorxiv/early/2025/10/19/2025.10.17.683190.full.pdf.

[14] Claar, L. D. *et al.* Cortico-thalamo-cortical interactions modulate electrically evoked EEG responses in mice. *eLife* **12**, RP84630 (2023). URL https://doi.org/10.7554/eLife.84630.

[15] Holze, F. *et al.* Direct comparison of the acute effects of lysergic acid diethylamide and psilocybin in a double-blind placebo-controlled study in healthy subjects. *Neuropsychopharmacology* **47**, 1180–1187 (2022). URL https://doi.org/10.1038/s41386-022-01297-2.

[16] Weinreb, C. *et al.* Keypoint-MoSeq: parsing behavior by linking point tracking to pose dynamics. *Nature Methods* **21**, 1329–1339 (2024). URL https://doi.org/10.1038/s41592-024-02318-2.

[17] Purple, R. J. *et al.* Short- and long-term modulation of rat prefrontal cortical activity following single doses of psilocybin. *Molecular Psychiatry* **30**, 5889–5900 (2025). URL https://doi.org/10.1038/s41380-025-03182-y.

[18] Skyberg, R. J., Fields, C. W., Martins, D. M. & Niell, C. M. The impact of the serotonergic psychedelic DOI on active vision in freely moving mice. *bioRxiv* (2025). 2692-8205 Skyberg, Rolf J Orcid: 0000-0001-6196-0417 Fields, Christopher W Martins, Dylan M Orcid: 0000-0001-9458-2694 Niell, Cristopher M Orcid: 0000-0001-6283-3540 F32 EY032360/EY/NEI NIH HHS/United States R01 DA055439/DA/NIDA NIH HHS/United States R25 MH131653/MH/NIMH NIH HHS/United States RF1 NS127305/NS/NINDS NIH HHS/United States Journal Article Preprint United States 2025/11/24 bioRxiv [Preprint]. 2025 Oct 15:2025.10.14.682230. doi: 10.1101/2025.10.14.682230.

[19] Michaiel, A. M., Parker, P. R. L. & Niell, C. M. A Hallucinogenic Serotonin-2a Receptor Agonist Reduces Visual Response Gain and Alters Temporal Dynamics in Mouse V1. *Cell Rep* **26**, 3475–3483.e4 (2019). 2211-1247 Michaiel, Angie M Parker, Philip R L Niell, Cristopher M F32 EY027696/EY/NEI NIH HHS/United States R01 EY023337/EY/NEI NIH HHS/United States T32 HD007348/HD/NICHD NIH HHS/United States Journal Article Research Support, N.I.H., Extramural United States Cell Rep. 2019 Mar 26;26(13):3475-3483.e4. doi: 10.1016/j.celrep.2019.02.104.

[20] Syeda, A. *et al.* Facemap: a framework for modeling neural activity based on orofacial tracking. *Nature Neuroscience* **27**, 187–195 (2024). URL https://doi.org/10.1038/s41593-023-01490-6.

[21] Bennett, C. *et al.* Shield: Skull-shaped hemispheric implants enabling large-scale electrophysiology datasets in the mouse brain. *Neuron* **112**, 2869–2885.e8 (2024). 1097-4199 Bennett, Corbett Ouellette, Ben Ramirez, Tamina K Cahoon, Alex Cabasco, Hannah Browning, Yoni Lakunina, Anna Lynch, Galen F McBride, Ethan G Belski, Hannah Gillis, Ryan Grasso, Conor Howard, Robert Johnson, Tye Loeffler, Henry Smith, Heston Sullivan, David Williford, Allison Caldejon,

Shiella Durand, Severine Gale, Samuel Guthrie, Alan Ha, Vivian Han, Warren Hardcastle, Ben Mochizuki, Chris Sridhar, Arjun Suarez, Lucas Swapp, Jackie Wilkes, Joshua Siegle, Joshua H Farrell, Colin Groblewski, Peter A Olsen, Shawn R Journal Article United States 2024/07/13 Neuron. 2024 Sep 4;112(17):2869-2885.e8. doi: 10.1016/j.neuron.2024.06.015. Epub 2024 Jul 11.

[22] Harris, J. A. *et al.* Hierarchical organization of cortical and thalamic connectivity. *Nature* **575**, 195–202 (2019). URL https://doi.org/10.1038/s41586-019-1716-z.

[23] Stringer, C., Michaelos, M., Tsyboulski, D., Lindo, S. E. & Pachitariu, M. High-precision coding in visual cortex. *Cell* **184**, 2767–2778.e15 (2021). URL https://doi.org/10.1016/j.cell.2021.03.042. Doi: 10.1016/j.cell.2021.03.042.

[24] White, C. M. *et al.* Psychedelic 5-HT2A agonist increases spontaneous and evoked 5-Hz oscillations in visual and retrosplenial cortex. *Communications Biology* **9**, 216 (2026). URL https://doi.org/10.1038/s42003-025-09492-9.

[25] Nestvogel, D. B. & McCormick, D. A. Visual thalamocortical mechanisms of waking state-dependent activity and alpha oscillations. *Neuron* **110**, 120–138.e4 (2022). 1097-4199 Nestvogel, Dennis B McCormick, David A R01 NS118461/NS/NINDS NIH HHS/United States R35 NS097287/NS/NINDS NIH HHS/United States RF1 NS118461/NS/NINDS NIH HHS/United States Journal Article Research Support, N.I.H., Extramural United States 2021/10/24 Neuron. 2022 Jan 5;110(1):120-138.e4. doi: 10.1016/j.neuron.2021.10.005. Epub 2021 Oct 22.

[26] Shao, L. X. *et al.* Psilocybin induces rapid and persistent growth of dendritic spines in frontal cortex in vivo. *Neuron* **109**, 2535–2544.e4 (2021). 1097-4199 Shao, Ling-Xiao Liao, Clara Gregg, Ian Davoudian, Pasha A Savalia, Neil K Delagarza, Kristina Kwan, Alex C R01 MH121848/MH/NIMH

NIH HHS/United States S10 OD023598/OD/NIH HHS/United States T32 GM007205/GM/NIGMS NIH HHS/United States T32 NS041228/NS/NINDS NIH HHS/United States Journal Article Research Support, N.I.H., Extramural Research Support, Non-U.S. Gov't United States 2021/07/07 Neuron. 2021 Aug 18;109(16):2535-2544.e4. doi: 10.1016/j.neuron.2021.06.008. Epub 2021 Jul 5.

[27] Brockett, A. T. & Francis, N. A. Psilocybin decreases neural responsiveness and increases functional connectivity while preserving pure-tone frequency selectivity in mouse auditory cortex. *J Neurophysiol* **132**, 45–53 (2024). 1522-1598 Brockett, Adam T Orcid: 0000-0001-7712-5053 Francis, Nikolas A Orcid: 0000-0001-6530-5559 GC30/University of Maryland (UMD)/ BBI/University of Maryland (UMD)/ Journal Article Research Support, Non-U.S. Gov't United States 2024/05/30 J Neurophysiol. 2024 Jul 1;132(1):45-53. doi: 10.1152/jn.00124.2024. Epub 2024 May 29.

[28] Halberstadt, A. L., Chatha, M., Klein, A. K., Wallach, J. & Brandt, S. D. Correlation between the potency of hallucinogens in the mouse head-twitch response assay and their behavioral and subjective effects in other species. *Neuropharmacology* **167**, 107933 (2020). 1873-7064 Halberstadt, Adam L Chatha, Muhammad Klein, Adam K Wallach, Jason Brandt, Simon D R01 DA041336/DA/NIDA NIH HHS/United States T32 MH018399/MH/NIMH NIH HHS/United States Journal Article Research Support, N.I.H., Extramural England 2020/01/10 Neuropharmacology. 2020 May 1;167:107933. doi: 10.1016/j.neuropharm.2019.107933. Epub 2020 Jan 7.

[29] Bradley, P. B., Elkes, C. & Elkes, J. On some effects of lysergic acid diethylamide (L.S.D. 25) in normal volunteers. *J Physiol* **121**, 50p–51p (1953). Bradley, p b Elkes, c Elkes, j Journal Article England 1953/08/01 J Physiol. 1953 Aug;121(2):50P-51P.

[30] Key, B. J. & Bradley, P. B. Effect of Drugs on Conditioning and Habituation to Arousal Stimuli in Animals. *Nature* **182**, 1517–1519 (1958). URL https://doi.org/10.1038/1821517a0.

[31] Lu, O. D. *et al.* A multi-institutional investigation of psilocybin's effects on mouse behavior. *bioRxiv* 2025.04.08.647810 (2025). URL https://www.biorxiv.org/content/biorxiv/early/2025/04/09/2025.04.08.647810.full.pdf.

[32] Roberts, B. F. *et al.* Effect of psilocybin on decision-making and motivation in the healthy rat. *Behav Brain Res* **440**, 114262 (2023). 1872-7549 Roberts, Brianna F Zylko, Alexia L Waters, Courtney E Crowder, Jessica D Gibbons, William J Jr Sen, Abhishek K Jones, J Andrew McMurray, Matthew S Journal Article Research Support, Non-U.S. Gov't Netherlands 2022/12/19 Behav Brain Res. 2023 Feb 25;440:114262. doi: 10.1016/j.bbr.2022.114262. Epub 2022 Dec 15.

[33] Torrado Pacheco, A., Olson, R. J., Garza, G. & Moghaddam, B. Acute psilocybin enhances cognitive flexibility in rats. *Neuropsychopharmacology* **48**, 1011–1020 (2023). URL https://doi.org/10.1038/s41386-023-01545-z.

[34] Horrocks, M., Mohn, J. L. & Jaramillo, S. The serotonergic psychedelic DOI impairs deviance detection in the auditory cortex. *J Neurophysiol* **133**, 388–398 (2025). 1522-1598 Horrocks, Max Orcid: 0009-0006-4201-8972 Mohn, Jennifer L Orcid: 0000-0002-6808-8489 Jaramillo, Santiago Orcid: 0000-0002-6595-8450 R01 NS118461/NS/NINDS NIH HHS/United States RF1 NS118461/NS/NINDS NIH HHS/United States R01NS118461/HHS | NIH | National Institute of Neurological Disorders and Stroke (NINDS)/ Journal Article United States 2024/12/27 J Neurophysiol. 2025 Feb 1;133(2):388-398. doi: 10.1152/jn.00411.2024. Epub 2024 Dec 27.

[35] Timmermann, C. *et al.* Lsd modulates effective connectivity and neural adaptation mechanisms in an auditory oddball paradigm. *Neuropharmacology* **142**, 251–262 (2018). URL https://www.sciencedirect.com/science/article/pii/S0028390817305063.

[36] Duerler, P. *et al.* Psilocybin Induces Aberrant Prediction Error Processing of Tactile Mismatch Responses—A Simultaneous EEG–FMRI Study. *Cerebral Cortex* **32**, 186–196 (2022). URL https://doi.org/10.1093/cercor/bhab202.

[37] Martin, D. A., Delgado, A. M. & Calu, D. J. Effects of psychedelic, DOI, on nucleus accumbens dopamine signaling to predictable rewards and cues in rats. *Neuropsychopharmacology* **49**, 1925–1933 (2024). 1740-634x Martin, David A Orcid: 0000-0001-5783-7141 Delgado, Angel M Calu, Donna J R01 DA043533/DA/NIDA NIH HHS/United States RO1DA043533/National Institute of Development Administration (NIDA)/ Journal Article England 2024/07/07 Neuropsychopharmacology. 2024 Nov;49(12):1925-1933. doi: 10.1038/s41386-024-01912-4. Epub 2024 Jul 6.

[38] Furutachi, S., Franklin, A. D., Aldea, A. M., Mrsic-Flogel, T. D. & Hofer, S. B. Cooperative thalamocortical circuit mechanism for sensory prediction errors. *Nature* **633**, 398–406 (2024). 1476-4687 Furutachi, Shohei Franklin, Alexis D Orcid: 0000-0002-6945-0830 Aldea, Andreea M Orcid: 0009-0003-2641-2302 Mrsic-Flogel, Thomas D Orcid: 0000-0002-8947-408x Hofer, Sonja B Orcid: 0000-0003-4921-8521 Osamu Hayaishi Memorial Scholarship/ Gatsby Charitable Foundation and Wellcome/ Journal Article Research Support, Non-U.S. Gov't England 2024/08/31 Nature. 2024 Sep;633(8029):398-406. doi: 10.1038/s41586-024-07851-w. Epub 2024 Aug 28.

[39] Hamm, J. P. & Yuste, R. Somatostatin Interneurons Control a Key Component of Mismatch Negativity in Mouse Visual Cortex. *Cell Reports* **16**, 597–604 (2016). URL https://www.sciencedirect.com/science/article/pii/S221112471630777X.

[40] Bastos, G. *et al.* Top-down input modulates visual context processing through an interneuron-specific circuit. *Cell Reports* **42** (2023). URL https://doi.org/10.1016/j.celrep.2023.113133. Doi: 10.1016/j.celrep.2023.113133.

[41] Natan, R. G. *et al.* Complementary control of sensory adaptation by two types of cortical interneurons. *eLife* **4**, e09868 (2015). URL https://doi.org/10.7554/eLife.09868.

[42] Iigaya, K., Fonseca, M. S., Murakami, M., Mainen, Z. F. & Dayan, P. An effect of serotonergic stimulation on learning rates for rewards apparent after long intertrial intervals. *Nat Commun* **9**, 2477 (2018). 2041-1723 Iigaya, Kiyohito Orcid: 0000-0002-4748-8432 Fonseca, Madalena S Murakami, Masayoshi Mainen, Zachary F Dayan, Peter Orcid: 0000-0003-3476-1839 250334/ERC_/European Research Council/International 671251/ERC_/European Research Council/International Journal Article Research Support, Non-U.S. Gov't England 2018/06/28 Nat Commun. 2018 Jun 26;9(1):2477. doi: 10.1038/s41467-018-04840-2.

[43] Matias, S., Lottem, E., Dugué, G. P. & Mainen, Z. F. Activity patterns of serotonin neurons underlying cognitive flexibility. *eLife* **6**, e20552 (2017). URL https://doi.org/10.7554/eLife.20552.

[44] Grossman, C. D., Bari, B. A. & Cohen, J. Y. Serotonin neurons modulate learning rate through uncertainty. *Curr Biol* **32**, 586–599.e7 (2022). 1879-0445 Grossman, Cooper D Bari, Bilal A Cohen, Jeremiah Y R01 DA042038/DA/NIDA NIH HHS/United States R01 NS104834/NS/NINDS NIH HHS/United States

Journal Article Research Support, N.I.H., Extramural Research Support, Non-U.S. Gov't England 2021/12/23 Curr Biol. 2022 Feb 7;32(3):586-599.e7. doi: 10.1016/j.cub.2021.12.006. Epub 2021 Dec 21.

[45] Hubert, F. *et al.* A state prediction error model explains serotonin activity and its role in cognitive flexibility. *Cosyne Abstracts 2026* (2026).

[46] Zhang, M. *et al.* Molecularly defined and spatially resolved cell atlas of the whole mouse brain. *Nature* **624**, 343–354 (2023). URL https://doi.org/10.1038/s41586-023-06808-9.

[47] Yao, Z. *et al.* A high-resolution transcriptomic and spatial atlas of cell types in the whole mouse brain. *Nature* **624**, 317–332 (2023). URL https://doi.org/10.1038/s41586-023-06812-z.

[48] De Filippo, R. & Schmitz, D. Transcriptomic mapping of the 5-HT receptor landscape. *Patterns* URL https://doi.org/10.1016/j.patter.2024.101048. Doi: 10.1016/j.patter.2024.101048.

[49] Davoudian, P. A. *et al.* Psilocybin reshapes cortical inhibition through selective interneuron recruitment. *bioRxiv* 2026.04.16.718963 (2026). URL https://www.biorxiv.org/content/biorxiv/early/2026/04/17/2026.04.16.718963.full.pdf.

[50] Schmitz, G. P. *et al.* Psychedelic compounds directly excite 5-HT2A layer V medial prefrontal cortex neurons through 5-HT2A Gq activation. *Translational Psychiatry* **15**, 381 (2025). URL https://doi.org/10.1038/s41398-025-03611-0.

[51] Ekins, T. G. *et al.* Cellular rules underlying psychedelic control of prefrontal pyramidal neurons. *bioRxiv* (2023). 2692-8205 Ekins, Tyler G Brooks, Isla Orcid: 0009-0000-6811-5873 Kailasa, Sameer Rybicki-Kler, Chloe Jedrasiak-Cape, Izabela Donoho, Ethan Mashour, George A Rech, Jason Ahmed, Omar J

Orcid: 0000-0003-3300-7658 R01 MH129282/MH/NIMH NIH HHS/United States T32 DA007268/DA/NIDA NIH HHS/United States Journal Article Preprint United States 2023/11/14 bioRxiv [Preprint]. 2023 Oct 23:2023.10.20.563334. doi: 10.1101/2023.10.20.563334.

[52] Vargas, M. V. *et al.* Psychedelics promote neuroplasticity through the activation of intracellular 5-HT2A receptors. *Science* **379**, 700–706 (2023). 1095-9203 Vargas, Maxemiliano V Orcid: 0000-0002-3637-1896 Dunlap, Lee E Orcid: 0000-0002-9365-8025 Dong, Chunyang Orcid: 0000-0002-4820-4454 Carter, Samuel J Orcid: 0000-0002-2276-4373 Tombari, Robert J Orcid: 0000-0002-6561-8181 Jami, Shekib A Orcid: 0000-0001-5478-1963 Cameron, Lindsay P Orcid: 0000-0002-8420-7898 Patel, Seona D Orcid: 0000-0001-8947-4533 Hennessey, Joseph J Orcid: 0000-0003-0981-4695 Saeger, Hannah N Orcid: 0000-0002-3055-5547 McCorvy, John D Orcid: 0000-0001-7555-9413 Gray, John A Orcid: 0000-0002-7287-0748 Tian, Lin Orcid: 0000-0001-7012-6926 Olson, David E Orcid: 0000-0002-4517-0543 P30 ES005707/ES/NIEHS NIH HHS/United States R35 GM133421/GM/NIGMS NIH HHS/United States R01 GM128997/GM/NIGMS NIH HHS/United States P50 HD103526/HD/NICHD NIH HHS/United States S10 OD025271/OD/NIH HHS/United States U01 NS120820/NS/NINDS NIH HHS/United States T32 GM099608/GM/NIGMS NIH HHS/United States S10 OD019980/OD/NIH HHS/United States R01 MH101214/MH/NIMH NIH HHS/United States T32 GM113770/GM/NIGMS NIH HHS/United States T32 MH112507/MH/NIMH NIH HHS/United States U54 HD079125/HD/NICHD NIH HHS/United States Journal Article United States 2023/02/17 Science. 2023 Feb 17;379(6633):700-706. doi: 10.1126/science.adf0435. Epub 2023 Feb 16.

[53] Fee, C., Banasr, M. & Sibille, E. Somatostatin-Positive Gamma-Aminobutyric Acid Interneuron Deficits in Depression: Cortical Microcircuit and Therapeutic Perspectives. *Biol Psychiatry* **82**, 549–559 (2017). 1873-2402 Fee, Corey Banasr, Mounira Sibille, Etienne R01 MH077159/MH/NIMH NIH HHS/United States Journal Article Review United States 2017/07/13 Biol Psychiatry. 2017 Oct 15;82(8):549-559. doi: 10.1016/j.biopsych.2017.05.024. Epub 2017 Jun 8.

[54] Guo, H. *et al.* Somatostatin-expressing neurons in the zona incerta regulate chronic stress response and modulate depression-like behaviors. *Molecular Psychiatry* (2026). URL https://doi.org/10.1038/s41380-026-03446-1.

[55] Fuchs, T. *et al.* Disinhibition of somatostatin-positive GABAergic interneurons results in an anxiolytic and antidepressant-like brain state. *Mol Psychiatry* **22**, 920–930 (2017). 1476-5578 Fuchs, T Jefferson, S J Hooper, A Orcid: 0000-0003-2977-3819 Yee, P-Hp Maguire, J Luscher, B R01 NS102937/NS/NINDS NIH HHS/United States R01 MH099851/MH/NIMH NIH HHS/United States R56 NS073574/NS/NINDS NIH HHS/United States R21 MH097247/MH/NIMH NIH HHS/United States T32 NS061764/NS/NINDS NIH HHS/United States R01 NS073574/NS/NINDS NIH HHS/United States Journal Article Research Support, N.I.H., Extramural England 2016/11/09 Mol Psychiatry. 2017 Jun;22(6):920-930. doi: 10.1038/mp.2016.188. Epub 2016 Nov 8.

[56] Anderson, K. M. *et al.* Convergent molecular, cellular, and cortical neuroimaging signatures of major depressive disorder. *Proceedings of the National Academy of Sciences* **117**, 25138–25149 (2020). URL https://doi.org/10.1073/pnas.2008004117. Doi: 10.1073/pnas.2008004117.

[57] Prévot, T. & Sibille, E. Altered GABA-mediated information processing and cognitive dysfunctions in depression and other brain disorders. *Molecular Psychiatry*

26, 151–167 (2021). URL https://doi.org/10.1038/s41380-020-0727-3.

[58] Barrett, L. F., Quigley, K. S. & Hamilton, P. An active inference theory of allostasis and interoception in depression. *Philosophical Transactions of the Royal Society B: Biological Sciences* **371**, 20160011 (2016). URL https://doi.org/10.1098/rstb.2016.0011. Doi: 10.1098/rstb.2016.0011.

[59] Buccino, A. P. *et al.* Spikeinterface, a unified framework for spike sorting. *Elife* **9** (2020). 2050-084x Buccino, Alessio P Orcid: 0000-0003-3661-527x Hurwitz, Cole L Orcid: 0000-0002-2023-1653 Garcia, Samuel Orcid: 0000-0001-6389-9779 Magland, Jeremy Orcid: 0000-0002-5286-4375 Siegle, Joshua H Orcid: 0000-0002-7736-4844 Hurwitz, Roger Hennig, Matthias H Orcid: 0000-0001-7270-5817 214431/Z/18/Z/WT_/Wellcome Trust/United Kingdom Journal Article Meta-Analysis Research Support, Non-U.S. Gov't England 2020/11/11 Elife. 2020 Nov 10;9:e61834. doi: 10.7554/eLife.61834.

[60] Birman, D. *et al.* Pinpoint: trajectory planning for multi-probe electrophysiology and injections in an interactive web-based 3d environment (2023). URL http://dx.doi.org/10.7554/eLife.91662.1.

[61] Juavinett, A. L., Nauhaus, I., Garrett, M. E., Zhuang, J. & Callaway, E. M. Automated identification of mouse visual areas with intrinsic signal imaging. *Nat Protoc* **12**, 32–43 (2017). 1750-2799 Juavinett, Ashley L Nauhaus, Ian Garrett, Marina E Zhuang, Jun Callaway, Edward M P30 EY019005/EY/NEI NIH HHS/United States R01 EY022577/EY/NEI NIH HHS/United States R01 MH063912/MH/NIMH NIH HHS/United States Journal Article England 2016/12/03 Nat Protoc. 2017 Jan;12(1):32-43. doi: 10.1038/nprot.2016.158. Epub 2016 Dec 1.

[62] Durand, S. *et al.* Acute head-fixed recordings in awake mice with multiple Neuropixels probes. *Nat Protoc* **18**, 424–457 (2023). 1750-2799 Durand, Séverine Orcid: 0000-0001-7788-0200 Heller, Greggory R Ramirez, Tamina K Luviano, Jennifer A Williford, Allison Sullivan, David T Cahoon, Alex J Farrell, Colin Orcid: 0000-0003-3487-3064 Groblewski, Peter A Bennett, Corbett Siegle, Joshua H Olsen, Shawn R Journal Article Research Support, Non-U.S. Gov't Review England 2022/12/09 Nat Protoc. 2023 Feb;18(2):424-457. doi: 10.1038/s41596-022-00768-6. Epub 2022 Dec 7.

[63] Jun, J. J. *et al.* Fully integrated silicon probes for high-density recording of neural activity. *Nature* **551**, 232–236 (2017). URL https://doi.org/10.1038/nature24636.

[64] Siegle, J. H. *et al.* Open Ephys: an open-source, plugin-based platform for multichannel electrophysiology. *J Neural Eng* **14**, 045003 (2017). 1741-2552 Siegle, Joshua H López, Aarón Cuevas Patel, Yogi A Abramov, Kirill Ohayon, Shay Voigts, Jakob Journal Article Research Support, Non-U.S. Gov't England 2017/02/09 J Neural Eng. 2017 Aug;14(4):045003. doi: 10.1088/1741-2552/aa5eea.

[65] Pachitariu, M., Sridhar, S., Pennington, J. & Stringer, C. Spike sorting with Kilosort4. *Nature Methods* **21**, 914–921 (2024). URL https://doi.org/10.1038/s41592-024-02232-7.

[66] Jain, A. *et al.* Unitrefine: A Community Toolbox for Automated Spike Sorting Curation. *bioRxiv* 2025.03.30.645770 (2025). URL https://www.biorxiv.org/content/biorxiv/early/2025/12/16/2025.03.30.645770.full.pdf.

[67] Myers, H. & Toglia, D. Whole Mouse Brain Delipidation - LifeCanvas Active v1 (2023). URL http://dx.doi.org/10.17504/protocols.io.rm7vzbz5rvx1/v1.

[68] Myers, H. & Toglia, D. Refractive Index Matching - EasyIndex v1 (2023). URL http://dx.doi.org/10.17504/protocols.io.kxygx965kg8j/v1.

[69] Myers, H. & Toglia, D. Whole Brain Embedding for SmartSPIM - EasyIndex with 2% Agarose v1 (2023). URL http://dx.doi.org/10.17504/protocols.io.3byl4jpn8lo5/v1.

[70] Mathis, A. *et al.* Deeplabcut: markerless pose estimation of user-defined body parts with deep learning. *Nature Neuroscience* **21**, 1281–1289 (2018). URL https://doi.org/10.1038/s41593-018-0209-y.

[71] Pedregosa, F. *et al.* Scikit-learn: Machine learning in Python. *the Journal of machine Learning research* **12**, 2825–2830 (2011).